

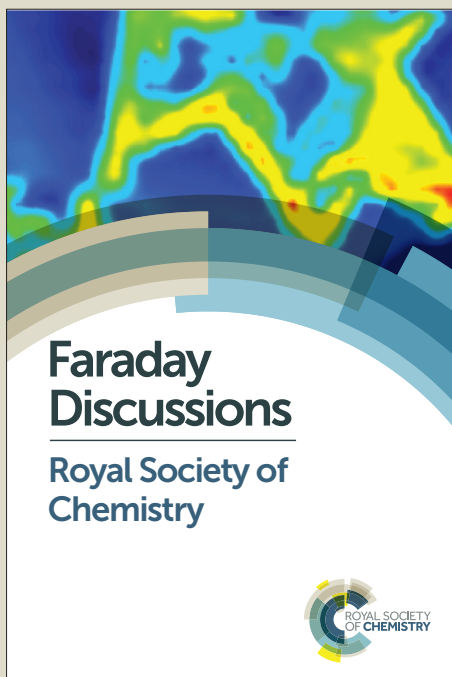
# Faraday Discussions

Accepted Manuscript



This manuscript will be presented and discussed at a forthcoming Faraday Discussion meeting. All delegates can contribute to the discussion which will be included in the final volume.

**Register now to attend!** Full details of all upcoming meetings: <http://rsc.li/fd-upcoming-meetings>



This is an *Accepted Manuscript*, which has been through the Royal Society of Chemistry peer review process and has been accepted for publication.

*Accepted Manuscripts* are published online shortly after acceptance, before technical editing, formatting and proof reading. Using this free service, authors can make their results available to the community, in citable form, before we publish the edited article. We will replace this *Accepted Manuscript* with the edited and formatted *Advance Article* as soon as it is available.

You can find more information about *Accepted Manuscripts* in the [Information for Authors](#).

Please note that technical editing may introduce minor changes to the text and/or graphics, which may alter content. The journal's standard [Terms & Conditions](#) and the [Ethical guidelines](#) still apply. In no event shall the Royal Society of Chemistry be held responsible for any errors or omissions in this *Accepted Manuscript* or any consequences arising from the use of any information it contains.

Cite this: DOI: 10.1039/c0xx00000x

www.rsc.org/xxxxxx

ARTICLE TYPE

# Role of edge geometry and chemistry in the electronic properties of graphene nanostructures

Shintaro Fujii,<sup>a†</sup> Maxim Ziatdinov,<sup>b†</sup> Misako Ohtsuka,<sup>a</sup> Koichi Kusakabe,<sup>c</sup> Manabu Kiguchi<sup>a</sup> and Toshiaki Enoki<sup>a</sup>

Received (in XXX, XXX) Xth XXXXXXXXX 20XX, Accepted Xth XXXXXXXXX 20XX

DOI: 10.1039/b000000x

The geometry and chemistry of graphene nanostructures significantly affect their electronic properties. Despite a large number of experimental and theoretical studies dealing with the geometrical shape-dependent electronic properties of graphene nanostructures, experimental characterisation of their chemistry is clearly lacking. This is mostly due to the difficulties in preparing chemically modified graphene nanostructures in a controlled manner and in identifying the exact chemistry of the graphene nanostructure on the atomic scale. Herein, we present scanning probe microscopic and first-principles characterisation of graphene nanostructures with different edge geometries and chemistry. Using the results of atomic scale electronic characterisation and theoretical simulation, we discuss the role of the edge geometry and chemistry on the electronic properties of graphene nanostructures with hydrogenated and oxidised linear edges at graphene boundaries and the internal edges of graphene vacancy defects. Atomic-scale details of the chemical composition have a strong impact on the electronic properties of graphene nanostructures, i.e., the presence or absence of nonbonding  $\pi$  states and the degree of resonance stability.

## Introduction

The electronic properties of graphene are crucially dependent on the geometrical shape and chemistry of its edge boundaries. Indeed, several experimental studies have demonstrated the dramatic influence of the crystallographic orientation of graphene one-dimensional edges (i.e., zigzag and armchair [Figure 1a]) on the electronic structure of graphene. According to current understanding, the zigzag edge of graphene supports the localised  $\pi$  state (edge state) on its boundary and gives rise to intra-valley scattering of extended electronic states. The edge state, which has a large local density of states in the edge region and is spin polarised, plays an important role in giving electronic, magnetic and chemical activities to zigzag edges. In contrast, its armchair counterpart does not possess the edge state and thus leads to inter-valley scattering of charge carriers.<sup>1-15</sup> The inter-valley scattering causes the formation of a standing wave, resulting in energetic stability in armchair edges. The electronic properties of graphene edges are also significantly affected by how foreign chemical species bond to the edge carbon atoms.<sup>6,16-30</sup> It is therefore appealing to tune electronic, magnetic and chemical properties of graphene-based nanostructures by changing the chemistry and geometrical shape of the graphene edge. In general, the chemistry of graphene nanostructures is poorly characterised on the atomic scale, largely due to the difficulty in controlling the chemistry at the edges and because of the poor chemical sensitivity of local probe methods such as scanning transmission

electron microscopy and scanning probe microscopy, although the situation is improving rapidly with increasing interest in graphene materials.<sup>10-15,31</sup> In order to better understand relationships between chemical and electronic properties in graphene nanostructures and to bring them to their possible practical applications, a number of studies including ours have succeeded in providing structural and electronic characterisations of representative and realistic graphene nanosystems in chemically and structurally well-defined samples.<sup>6,25-30</sup> Here we present our findings from scanning probe microscopy and first-principles characterisation of graphene nanostructures with different geometrical shapes and chemical compositions.

## Effect of geometry at the edge

Graphene is a zero-gap semiconductor and its low-energy  $\pi$  state is characterised by electron-hole symmetry and linear conduction and valence bands within the nearest-neighbour tight-binding approximation.<sup>11,13,31</sup> The unit cell of graphene contains two physically non-equivalent carbon atoms denoted as A and B atoms [Figure 1a]. From a chemical perspective, graphene is a large polyaromatic hydrocarbon, and it can be represented by the resonance of three degenerate Clar formulas with fully benzenoid characters<sup>32</sup> [Figure 1b]. Thus graphene is essentially an inert material, but the introduction of boundaries into the bulk graphene drastically affects the chemical reactivity and the electronic properties around the boundaries. We start by

introducing the most typical graphene boundaries of a one-dimensional linear edge. When the graphene is cut along fundamental crystallographic directions and hydrogen atoms are attached to each edge carbon atom, two main types of linear edges, called armchair and zigzag shapes, are generated, as shown in Figures 1c and d, respectively. The local chemical structure around the armchair-shaped edge can be represented by a unique Clar formula<sup>32</sup> with a thermodynamically stable (*i.e.*, fully benzenoid) character. The non-uniform sextet distribution (localisation of the sextet) is in sharp contrast to that of bulk graphene, in which the sextet migrates over the honeycomb lattice to form uniform  $\pi$ -electron distribution.<sup>31</sup> In contrast, the local chemical structure around the zigzag-shaped edge is described by the resonance of three degenerated formulas with chemically reactive radical characters at the edge sites (*i.e.*, non-Kekulé type Clar formulas). In addition to the radical character at the edge site, the sextet migration in the resonance leads to uniform sextet distribution, as in the case of bulk graphene. The unit cell of the degenerated Clar formulas around the zigzag-shaped edge contains three edge sites, and an unpaired electron is localised at one of these three edge sites.

We can understand the edge-geometry-induced modification of the electronic features on the basis of the physics of the two-dimensional graphene–bipartite lattice, in which electrons move with their behaviour as upon massless Dirac fermion, as given by Weyl equation;

$$\hat{H} = v_F \sigma \mathbf{p}, \quad (\text{eq. 1})$$

where  $v_F$ ,  $\sigma$  and  $\mathbf{p}$  are the Fermi velocity, the Pauli matrix of the pseudo-spin, and the momentum, respectively.<sup>13</sup> The pseudo-spin appears upon from the equivalence of the structural degree of freedom 2 in the A/B bipartite lattice to the spin degree of freedom  $\uparrow\downarrow$ . Two sets of linear conduction and valence bands (Dirac cones) are created at K and K' points in the Brillouin zone, due to the biparticity of the lattice [Figure 1e]. The fully benzenoid structure of the armchair edge originates from the formation of a standing wave as a consequence of electron wave interference, which is due to the inter-valley scattering at the armchair edge, in which K and K' points participate. In contrast, the presence of unpaired electrons is caused by the broken symmetry of the pseudo-spin of the massless Dirac fermion at the zigzag edges (*i.e.*, the broken symmetry between the A and B sublattices in the bipartite system).<sup>13</sup> As shown in the bipartite models in Figures 1f and 1g, the local sublattice symmetry at the graphene boundaries consisting of secondary carbon sites is broken for the zigzag edge, whereas the A and B sublattices are always paired for the armchair boundary. Figures 2a and b show band structures for graphene nanoribbon models with hydrogenated armchair and zigzag edges, respectively. The gap opening for the armchair model and the flat bands near the Brillouin-zone boundary for the zigzag model (see the band dispersion at  $(2/3)\pi < k < \pi$ ), respectively, manifest the benzenoid and edge-localised radical characters,<sup>1,2</sup> as predicted in the corresponding Clar formulas. It should be noted here that beyond the two typical armchair- and zigzag-shaped edges, local probe analysis on chiral-shaped edges prepared by the unzipping of carbon nanotubes has been reported recently.<sup>25,33</sup>

## Discussion

The chemistry at the edge has a remarkable impact on the electronic structure near the graphene edge. Understanding the chemistry has been a long-standing problem, and it is mostly discussed based on theoretical models.<sup>16–20</sup> However, it is still a challenging task to realize the chemical modification of a graphene edge and to tune the electronic properties in a controlled manner. In response to the challenge, several local probe analyses of chemically modified graphene edges in combination with bottom-up synthesis and nano-fabrication techniques have been reported recently.<sup>6,15,21–27,29</sup> We too have focused on scanning probe characterisation of chemically modified graphene edges in order to study the effect of the chemistry on the electronic properties of graphene.<sup>6,22,24,25</sup> In the following, we discuss the effect of hydrogenation and oxidation on the electronic structure of graphene edges by referring to the model structures of zigzag and armchair edges described above (Figures 1 and 2).

### Effect of chemistry at the edge

Hydrogenated graphene edges with atomically smooth boundaries contained within nano-sized pits were prepared by atomic hydrogen etching of single vacancies in the topmost graphene layer of graphite.<sup>6</sup> To simulate scanning probe microscopic (STM) images and corresponding tunnelling spectroscopy data, electronic calculations based on density functional theory (DFT) were performed. High-resolution STM characterisations and DFT simulations demonstrate that atomically well-defined mono-hydrogenated zigzag edges are preferentially formed at the periphery of the nanoholes with mono-atomic depth, as shown in Figures 3a and b. As predicted in the DFT simulation, the low-energy STM contrast with bright spots at the zigzag-shaped edge is dominated by an edge-localised non-bonding  $\pi$  state at the boundary [Figures 3b and c], which reflects the  $\pi$ -radical character [Figure 1d] and is due to the higher local density of states (LDOS) originating from the flat band [Figure 2b]. The edge-localised state decays into bulk quickly to form an  $a \times a$  periodic pattern ( $a$ : lattice constant (0.246 nm) in the graphene–bipartite lattice [Figure 3b]). The edge-localised non-bonding state, which is also called an edge state,<sup>1,2</sup> can be a source of electronic and magnetic activity, and thus the potential application of the edge-localised non-bonding state functionalised in graphene materials has long been discussed in the nanocarbon community.<sup>10–15</sup> The results of our scanning tunnelling spectroscopy on the hydrogenated zigzag edge suggests that a spin gap is formed as a result of ferromagnetic ordering of the magnetic moment along the zigzag edge sites,<sup>6</sup> which puts forward the potential electronic and magnetic functionalisation of graphene-based materials with controlled edge-chemistry. It is noteworthy that the size of the spin gap is sensitive to the details of edge preparation and hence its chemistry. Indeed, the spin gap reported for the oxidised edges of unzipped carbon nanotubes, reconstructed edges in chemical vapour deposition-grown graphene ribbons, and hydrogen-etched edges in graphite nanoholes is 0.03–0.05 eV,<sup>34</sup> 0.05–0.08 eV,<sup>33</sup> and 0.16 eV,<sup>6</sup> respectively.

Hydrogenated armchair-shaped edges were prepared by hydrogenation of the graphene edges on graphite. The electronic

state around the armchair-shaped edge is characterised by extended  $\pi$  states with superperiodic pattern with  $\sqrt{3}a \times \sqrt{3}a$  periodicity [Figures 4a and b], which is associated with the non-uniform sextet distribution (sextet localisation) [Figure 1c] and can be interpreted as a result of inter-valley scattering of low-energy electron waves and the resultant interference patterns with charge-density wave (CDW) formation around the edge.<sup>7-9</sup>

In addition to the conventional mono-hydrogenated zigzag edge, we found a new type of zigzag edge on the periphery of the nanohole, which was characterised by the disappearance of the edge-localised state and instead by the formation of superperiodic pattern with  $\sqrt{3}a \times \sqrt{3}a$  periodicity [Figure 3d]. The structure of the superperiodic pattern mimics that around the armchair-shaped edges with a thermodynamically stable character, which implies non-uniform sextet distribution and inter-valley scattering around the edge.

To understand these two main features, we have to take into account the chemistry at the zigzag edge. Systematic DFT simulations show that the edge-localised state can be removed when every third zigzag-edge site is di-hydrogenated while the other two sites remain mono-hydrogenated [Figure 3e]. The DFT simulation reproduces the absence of the localised state at the edge sites, as well as the presence of the extended superperiodic  $\sqrt{3}a \times \sqrt{3}a$  patterns (*i.e.*, CDW formation) around the boundary in the STM image [Figure 3e]. A previous DFT study of a variety of hydrogenated graphene edges already demonstrated that the partially di-hydrogenated zigzag edge is energetically stable.<sup>20</sup> The partially di-hydrogenated zigzag edge can be represented by a Kekulé-type Clar formula, in which radical characters of the original mono-hydrogenated edge are quenched by attachment of an additional (second) hydrogen atom to every third carbon site [Figure 5a]. The non-uniform sextet migration gives the localised character of the sextet distribution [Figure 5b], which can be associated with the superperiodic distribution of the  $\pi$  electrons. The DFT-calculated band structure confirms the disappearance of the flat bands around the Fermi energy  $E_F$  and the opening of the gap [Figure 6a]. The local sublattice symmetry of the partially di-hydrogenated zigzag boundary can be intuitively understood from the effective bipartite model, in which the number of the A and B sublattice sites at the boundary is balanced [Figure 5c].

In addition to the two main types of hydrogenated zigzag edges, some fraction (less than 5%) of the short zigzag edges with atomically smooth boundaries features unconventional  $\pi$ -state distribution, in which one can recognise a weak amplitude at the edge sites [Figure 3f]. We attributed this structure to fully di-hydrogenated zigzag edges (also known as Klein edges<sup>35,36</sup>). The observed STM image and DFT simulation show a reasonable match [Figures 3f and 3g]. In a manner similar to that of the mono-hydrogenated zigzag edge, the fully di-hydrogenated edge can be represented by resonance of three degenerated Clar formulas with radical characters at the bearded edge sites [Figure 5d]. The unit cell of the degenerated Clar formulas contains three edge sites, and two unpaired electrons are localised at two of the three edge sites. In a crude discussion, the degree of the radical character is two times higher for the di-hydrogenated edge than for the mono-hydrogenated edge (*i.e.*, the unit cell contains an unpaired electron, which is shared by three edge-carbon sites for

the mono-hydrogenated edge, whereas two unpaired electrons are shared by three edge-carbon sites for the di-hydrogenated edge). The higher degree of the radical character, that is, the larger density of states of the edge-localised state, is evident in the DFT band structures of the graphene nanoribbon models. Figure 6b shows band structures for graphene nanoribbon models terminated by the di-hydrogenated zigzag edge. In contrast to the mono-hydrogenated zigzag edge, flat bands appear at  $0 < k < (2/3)\pi$ , indicating that the density of states is approximately two times larger than that of the mono-hydrogenated edge ( $(2/3)\pi < k < \pi$ ). The bipartite model suggests that the local sublattice symmetry is broken at the fully di-hydrogenated edge where the boundary is terminated by one of the sublattices [Figure 5e].

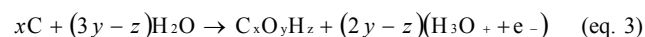
The di-hydrogenated zigzag edge can gain energetic stability *via* a hyperconjugation-type interaction.<sup>36,37</sup> The hyperconjugation originates from the interaction of the electrons in a  $\sigma$  bond (C–H bond at the di-hydrogenated site) with an adjacent  $p_z$  orbital in graphene, leading to an extended  $\pi$ -electron network. In the corresponding Clar formulas, two unpaired electrons participate in the graphene  $\pi$ -electron network by forming additional aromatic sextets, which leads to resonance stabilisation [Figure 5f]. The interaction between the electrons in the C–H bond and  $p_z$  orbital causes a finite increase in the amplitude of the localised state at the di-hydrogenated moiety in the DFT simulation [Figure 3g]. We believe that the bearded  $\pi$  state in the STM image in Figure 3f is strong indication of the hyperconjugation-type interaction.‡

To further investigate the effect of chemistry on the electronic properties of graphene edges, we investigated the effect of oxidation. The oxidised structure is commonly present in real-world graphene materials that are in contact with an ambient environment during their preparation process. In our studies, the oxidised graphene edges with atomically smooth edge boundaries were prepared by electrochemical oxidation of a graphitic surface.<sup>26</sup> The electrochemical oxidation preferentially proceeds at the graphene edges and leads to fragmentation of the graphitic surface [Figure 7a]. A closer examination of the atomic-scale STM images of the nano-fragment revealed that not only ragged edge boundaries but also atomically sharp edge boundaries that terminated along a zigzag direction were present on the periphery of the nanographene fragments [Figure 7b]. In sharp contrast to the conventional hydrogenated graphene edge, electrochemically oxidised edges (carboxylated edges in this study) with higher thermodynamic stability exhibited significantly modulated  $\pi$  states near the Fermi level [Figure 6c], which is characterised by a quasi-localised edge state with a spatially extended character in both the experiment and the DFT simulation [Figure 7c]. Although the mono-hydrogenated zigzag edge features strongly edge-localised  $\pi$  states at several sublattice sites from the boundary, the quasi-localised state in the oxidised edge decays into bulk up to 2 nm. This modulation can be understood in terms of the participation of the oxygen  $\pi$ -electrons into the graphene  $\pi$ -electron system and the change in the effective boundary conditions of the  $\pi$  electron network, as predicted previously.<sup>38</sup> The carboxylated edge can be represented by the resonance of three degenerated Clar formulas with radical characters at the oxygen edge sites [Figure 8a]. The  $\pi$ -electron network and corresponding bipartite model [Figure 8b] are similar to those of

the fully di-hydrogenated edge (*i.e.*, Klein type) in terms of the effective geometry of the network.

A remarkable difference between the two Klein-type edges of the di-hydrogenated edge and the carboxylated edge is the energy dispersion of the low-energy  $\pi$  state (flat bands near  $E_F$ ) [Figure 6c]. The oxygen atoms at the bearded site of the carboxylated edge with higher electronegativity induces band bending *via* the charge-transfer effect,<sup>22,26</sup> which causes a quasi edge-localised state with a spatially extended character. Calculation of the free energy (eq. 2) of the expected hydrolysis reaction in our electrochemical oxidation process (eq. 3), as described below, revealed that the observed carboxylated edge was in fact the most favourable edge under electrochemical potentials from 0.8 to 1.7 V (RHE (reversible hydrogen electrode)) [Figure 7d].

$$\Delta G = E_{C_xO_yH_z} + (2y - z)(E_{H_3O^+} + RT \ln a(H_3O^+)) + E_F - F\Delta\phi - xE_c - (3y - z)E_{H_2O} \quad (\text{eq. 2})$$



Here  $E_{C_xO_yH_z}$  is the DFT-calculated total energy of the graphene nanoribbon model with the chemical composition of  $C_xO_yH_z$ . The values  $E_c$ ,  $E_{H_3O^+}$ , and  $E_{H_2O}$  are the total energies of bulk carbon,  $H_3O^+$ , and  $H_2O$ , respectively,  $F$  is the Faraday constant,  $\Delta\phi$  is the electrochemical potential, and  $a$  is the activity. The oxidised linear zigzag edge is stable in air and could be one of designs to functionalize graphene nanostructures based on the edge-related unique electronic states.<sup>‡†</sup>

## Effect of chemistry at point defects

Although the number of studies dealing with the chemistry of one-dimensional linear edges has continuously increased in recent years, there is a significant lack of experimental and theoretical studies on the chemistry of point defects (*i.e.*, zero-dimension vacancy-internal edges). In a manner similar to that of the one-dimensional edge, the geometry and chemistry of the zero-dimensional vacancy-internal edges could affect the electronic properties.

A majority of the atomic-scale characterisations of point defects have focused on several model systems, such as pristine and/or reconstructed pristine vacancy defects.<sup>11</sup> In contrast to the case of the one-dimensional edge, adsorption of foreign chemical species on vacancy-internal edges induces large out-of-plane deformation of the graphene plane around the defects, which would lead to the formation of several metastable structures, as we will see in the following discussion.

Hydrogenated single vacancies were prepared by exposing non-passivated single vacancies [Figure 9a] to an atomic hydrogen environment.<sup>28</sup> After the hydrogenation process, the single vacancies showed significant changes in the electronic state near the vacancy sites, which are characterised by two main types of electronic states [Figures 9b and 9c].

The non-passivated single vacancy has three undercoordinated carbon atoms with  $\sigma$ -dangling bonds. Each undercoordinated carbon can in principle accommodate up to two hydrogen atoms. To simulate the possible structures of the

hydrogenated vacancies, systematic DFT calculations were performed, in which a variety of hydrogenated structures are evident [Figure 10a]. Free-energy analysis of the possible metastable structures reveals that there are two preferential hydrogenated vacancy structures, within our preparation conditions, V(111) and V(211) [Figure 10b]. The free energy  $G_H$  is calculated as

$$G_H = (E_{V_{n1, n2, n3}} - E_V - n_H \times E_H) - N_H \times \mu_H \quad (\text{eq. 4})$$

where  $E_{V_{n1, n2, n3}}$ ,  $E_V$ ,  $E_H$  are the total energies of a hydrogenated atomic vacancy (the indices  $n1$ ,  $n2$ , and  $n3$  denote the number of hydrogen atoms attached to each of the vacancy's undercoordinated carbon atoms), the non-passivated vacancy, and an isolated hydrogen atom, respectively, whereas  $n_H$  stands for the total number of hydrogen atoms in the vacancy and  $\mu_H$  stands for the chemical potential. One can see a good match between the experimental STM data [Figures 9b and 9c] and the DFT simulations [Figures 9d and 9e]. The preferable hydrogenated vacancy structures are characterised by the emergence and disappearance of the vacancy-internal edge localised  $\pi$  state (a flat band near  $E_F$ ) for fully mono-hydrogenated (V(111)) and partially di-hydrogenated (V(211)) vacancies, respectively [Figures 11a and b].

Lieb's theorem predicts the total spin of the ground state of the Hubbard model in graphene-bipartite lattices.<sup>39</sup> The total spin  $S$  of the ground state is  $S = (N_A - N_B)/2$  where  $N_A$  and  $N_B$  are the numbers of carbon-sites belonging to A and B sublattices, which indicates that the edge-localised non-bonding state appears if the sublattice symmetry is broken. The sublattice symmetry of the fully mono-hydrogenated and partially di-hydrogenated edges can be respectively estimated to be imbalanced and balanced [Figures 11c and d], *i.e.*,

$$N_{\text{bulk}}(C_A + C_B) - C_{A\_vacancy} = (N_{\text{bulk}} - 1)(C_A + C_B) + C_B$$

for V(111)

$$(N_{\text{bulk}} - 1)(C_A + C_B) + C_B - C_{B\_CH_2} = (N_{\text{bulk}} - 1)(C_A + C_B)$$

for V(211)

where  $N_{\text{bulk}}$  is the number of A–B paired bulk carbons of  $C_A$  and  $C_B$ ,  $C_{A\_vacancy}$  is the A sublattice of the vacancy site, and  $C_{B\_CH_2}$  is the sublattice of the di-hydrogenated carbon site. These findings again confirm that the chemistry at the graphene edge is inevitably linked to the unique  $\pi$  state and related electronic functionalities in the graphene materials.

There has been much interest in a point defect-induced magnetism in graphene materials.<sup>11</sup> The defect induced magnetism has been addressed in a considerable number of theoretical works, in which non-passivated single vacancy and partially hydrogenated single vacancies (*i.e.*, V(000),<sup>11,17,18</sup> V(100),<sup>17</sup> V(111)<sup>17</sup> and V(110)<sup>18</sup> in our notation) are used as model system. The V(111) model has been considered to be the most unlikely case in the previous paper<sup>17</sup> possibly due to undesirable steric hindrance effects among the hydrogen atoms at the vacancy. Thus the point defect-induced magnetism for the

V(111) model has not been well addressed yet. In our previous paper,<sup>6</sup> the plane wave-based LSDA calculations within Quantum ESPRESSO code<sup>40</sup> suggested that magnetic moment associated with the point defect of V(111) vanishes at the sufficiently large supercell size. In the current work we address the magnetic properties of the V(111) complex by adapting the strictly localized basis sets as implemented in the SIESTA code.<sup>41</sup> The generalized gradient approximation (GGA) exchange-correlation density functional<sup>42</sup> was employed together with a double- $\zeta$  plus polarization basis set, norm-conserving pseudopotentials, and a mesh cutoff of 200-400 Ry. For the Brillouin zone integrations a  $10 \times 10 \times 1$  Monkhorst-Pack  $k$ -mesh<sup>43</sup> was used. The spin-polarized calculations show that the defect-induced  $\pi$ -localized state of the V(111) complex has a magnetic moment of *ca.*  $1 \mu_B$ , which is coupled to the magnetic moments in the neighboring supercells via the ferrimagnetic superexchange interaction for supercell models of  $4a \times 4a$  and  $9a \times 9a$  ( $a$  = graphene lattice constant). The calculated band structures [Figures 11e and 11f] exhibit spin gap formation of *ca.* 320 and 70 meV at the Dirac point for the  $4a \times 4a$  and  $9a \times 9a$  models, respectively. The spin-polarized states are *ca.* 50 and 70 meV more stable than paramagnetic ones for the  $4a \times 4a$  and  $9a \times 9a$  models, respectively. In a striking contrast to the V(000) and V(100) models in which magnetic moments vanish along with increasing the supercell size (*i.e.*, decreasing defect density), the V(111) models preserves a magnetic moment of  $1 \mu_B$  at the sufficiently large supercell sizes of  $8a \times 8a$ ,  $9a \times 9a$  and  $12a \times 12a$  (*i.e.*, at low defect densities). This result within DFT calculations of the single defect models in periodic supercells has important implications for defect-induced magnetism based on chemical modification as it provides a possible route to design a magnetic state in graphene even at relatively low density of the vacancy defects.

Typically, the non-passivated single vacancy model has been used to explain observed single-vacancy-related phenomena such as the emergence of the vacancy-internal-edge-localised  $\pi$  state and its interaction with conduction electrons (*e.g.*, the Kondo effect and magnetic ordering associated with the localised  $\pi$  state<sup>11,44</sup>). As we have seen above, small variations in the atomic details at the linear and vacancy-internal edges, which is how chemical species are attached to the edges, have a considerable impact on the electronic structure. This is a natural consequence of the chemistry at the graphene edge in realistic samples; however, it has not been considered seriously, which is most likely due to the apparent complexity in edge-chemical compositions. In striking contrast to the chemical modification of monovalent hydrogen atoms, oxidation of the vacancy-internal edges introduces apparent complexity into the system because of the variation in the oxygen bonding patterns; nevertheless, we could treat this issue and consider realistic chemistry at the edge with the aid of DFT simulations.

Oxidised vacancy defects were prepared by chemical and thermal reduction of single-layered oxidised graphene on Au(111).<sup>27</sup> After the removal of the oxygen functional groups on the oxidised graphene, the remaining oxidised vacancy-defects featured vacancy-internal-edge-localised states with an apparent size of several nanometers [Figure 12a]. Interestingly, some fraction of the defects exhibited dynamical ON-OFF switching of

the vacancy-internal-edge-localised states, which can be induced by scanning probe manipulation. During raster scanning from the top to the bottom of the image, the vacancy-internal-edge-localised state is manipulated from ON to OFF when the scanning probe is scanned across the defect site [Figure 12b]. The switching proceeds reversibly (*i.e.*, from ON to OFF and from OFF to ON). To identify the oxidised defects subject to the reversible switching, DFT modelling was performed in a manner similar to the hydrogenated vacancy modelling. Here we consider oxidised mono- and di-vacancy models to reproduce the reversible ON-OFF switching of the vacancy-internal-edge-localised state and corresponding reversible structural change between two metastable configurations. The systematic DFT simulation within the oxidised vacancy models revealed that only a limited number of models can explain the reversible switching of the vacancy-internal-edge-localised state. Transition-state calculations based on the linear synchronous transit/quadratic synchronous transit (LST/QST) algorithm indicated that Model 2 of the oxidised di-vacancy with an activation barrier of  $<1$  eV is the most probable among the considered structures within the LDA calculations<sup>27</sup> [Figure 13]. The ON-OFF switching is caused by the change in the oxygen-bonding patterns, where two carbonyl groups are changed into two ether (epoxy) groups in a concerted fashion [Figure 14a]. The cooperative reaction essentially reduces the reaction barrier height between the two states ( $<1$  eV), which act as a moderate barrier to separate the two states and enables the reaction to be manipulated (*i.e.*, ON-OFF switching of the edge-localised states) by scanning probe.

The ON-OFF switching of the defect-localised states can be intuitively understood in terms of the sublattice symmetry. Based on the simple consideration that the  $\pi$  electrons in the ether group have nothing to do with the graphene  $\pi$ -electron network, the carbonyl group adds an additional  $\pi$  electron to the graphene  $\pi$  system and the epoxy group removes two  $\pi$  electrons from the neighbouring sublattice sites. Bipartite models of the ON and OFF states are shown in Figure 14b. The sublattice symmetry of the ON and OFF states can be respectively described to be imbalanced and balanced, *i.e.*,

$$N_{\text{bulk}} (C_A + C_B) - (C_A + C_B)_{\text{divacancy}} + 2 C_{A,\text{carbonyl}} = (N_{\text{bulk}} - 1)(C_A + C_B) + 2 C_A$$

for ON state

$$N_{\text{bulk}} (C_A + C_B) - (C_A + C_B)_{\text{divacancy}} - (C_A + C_B)_{\text{epoxy}} = (N_{\text{bulk}} - 2)(C_A + C_B)$$

for OFF state

where  $N_{\text{bulk}}$  is the number of the A-B-paired bulk carbons of  $C_A$  and  $C_B$ ,  $-(C_A+C_B)_{\text{divacancy}}$  stands for the removal of the A-B-paired sublattice sites due to di-vacancy-generation,  $+C_{A,\text{carbonyl}}$  is the addition of the A sublattice site corresponding to the attachment carbonyl group, and  $-(C_A+C_B)_{\text{epoxy}}$  stands for the removal of the A-B-paired sublattice sites due to epoxy adsorption.

DFT-calculated band structures confirm that the ON state is

characterised by quasi-flat dual bands (*i.e.*, imbalance = +2  $C_A$ ) crossing the Fermi level, whereas the OFF state does not have a flat band (*i.e.*, imbalance = 0) [Figure 15]. DFT simulation indicates that the ON state has the edge-localised  $\pi$  state strongly localised at the vacancy-internal edge sites, which decay into the bulk with a finite amplitude at one of the graphene sublattice sites with the  $a \times a$  periodicity, whereas the edge-localised  $\pi$  state is quenched for the OFF state, in which an extended  $\pi$  state propagates around the defect region to form a superperiodic pattern of  $\sqrt{3}a \times \sqrt{3}a$  periodicity [Figure 15]. A closer examination of the simulated STM-isosurface reveals that the decaying  $\pi$ -state distribution with the  $a \times a$  periodicity for the ON state and the extended  $\pi$  state with  $\sqrt{3}a \times \sqrt{3}a$  periodicity for the OFF state correlate well with the experimentally observed patterns. The triangular pattern of the edge-localised state in the ON state is in qualitative agreement with the experimental data, whereas the complete disappearance of the edge-localised state in the OFF state is evident from both theoretical and experimental results.

The switching of the electronic activity is promoting further arguments. As well-known, the effective Hamiltonian of graphene, *i.e.*, the low-energy effective Dirac field theory (Weyl equation of (eq. 1) or the  $k \cdot p$  theory) and the tight-binding Hamiltonian for the  $\pi$  electron system, is classified by its time-reversal symmetry and the particle conservation.<sup>45</sup> The topological number appears as a winding number, representing the topological charge. The topological quantum number is insensitive to disorder (deformation of graphene plane), indemnifying a defined state (ON or OFF) against loss of the information. Then, the switching is naturally realized by chemistry-induced modulation only, where the charge topological number (the particle number) is switched. The action is defined in the microscopic scale and thus it is expected to be controllable more stable than a method using bias controlled charge modulation. All of examples shown in this paper prove that the chemical control of “edge mode” is enhancing our possibility to tune the electronic, magnetic, and chemical properties of graphene and related nanostructures in various preferable manners.

### Stability of the edge mode in nanoscale graphene corners

We have previously studied electronic properties of the edge-localized state in the quasi-isolated linear edges with several nano-meter lengths. Here we focus on the properties of the edge mode along the nanoscale corner edges in graphene. We are particularly interested in the corner structures in graphene nanosized two-dimensional holes. The nanohole structures have attracted much interest because of the possibility to introduce effectively edge structures into bulk graphene to modify its electronic properties. Of specific interest are the so-called graphene nano-mesh and antidote lattices. It has been argued that lattice scale irregularities in the nanoholes can significantly affect the spin transport through the antidote lattices.<sup>46</sup> Therefore, atomic-scale experimental data on the properties of nanoholes can be crucial for a future spintronic devices. We have recently

succeeded in preparing nanosized hole-structures with atomically smooth edges by combination of the Ar ion sputtering and following atomic hydrogen-etching of graphitic surface<sup>6</sup> [Figures 16a and 16b]. The hole-edges are terminated along zigzag directions and emergence of the edge-localized state at the hole-edges is characterised as increased LDOS around the nanohole [Figure 16a]. The hole structure possess corners where two linear hole-edges are interconnected at the corner sites and thus a simple question arises: Do the low energy edge-localized states appear at the site that interconnects two edges? To answer this question, we analyzed the distribution of the edge-localized states in the corners of the nanoholes. We are particularly interested in the monohydrogenated edges, whose properties can be well compared with the effective mass description of the electronic properties of the graphene corner edges.<sup>47</sup> The representative constant current STM images of the nanoholes with the zoomed up areas of 150°, 120°, 60° nanoscale edge corners are shown in Figures 16i-16iii. The individual bright spots associating with the edge state, as described earlier, can be distinguished at the edges of these nanoholes at lower bias voltages and higher tunnelling currents. DFT structural realizations were performed using SIESTA code<sup>41</sup> with a double- $\zeta$  plus polarization basis set, norm-conserving pseudopotentials, a mesh cutoff of 200Ry and  $2 \times 2 \times 1$  Monkhorst-Pack  $k$ -mesh. All atoms were fully relaxed until the forces were less than 0.01 eV/Å. Simulations of STM isosurface was obtained for the relaxed atomic positions using Quantum Espresso code<sup>40</sup> at the LDA level. The electron-ion interaction was described by the projector augmented-wave method.<sup>48</sup> The wave function cutoff energy was set of 40 Ry. The Brillouin zone integration was performed using a uniform  $4 \times 4 \times 1$  Monkhorst-type  $k$ -point grid. We assume a quasi-flat geometry of the edges, noting that the small out of the plane bending of the monohydrogenated edge does not affect the appearance of the edge state in the constant current STM image as discussed previously.<sup>6</sup> We therefore work within the framework of the Tersoff-Hamann approximation,<sup>49,50</sup> where the STM data at relatively low bias voltages represents contour maps of constant surface LDOS at the Fermi energy. We found a significant decrease in the LDOS at all the edge corners [Figures 16i and 16ii], which can be interpreted as a disappearance of the edge-localized states in these corners. The absence of the edge state in the 150° and 120° corners is in a good agreement with theoretical predictions based on the effective mass approximation<sup>47</sup> and DFT theory.<sup>51</sup> On the other hand, absence of the edge state features in 60° corner edge [Figure 16iii] looks surprising and deviates from predictions of the effective mass scheme. To understand this discrepancy we first point out that in a non-relaxed structure of 60° corner, two hydrogen atoms are located very close to each other. We therefore examined more realistic chemistry at the corners and calculated charge density distribution in three possible structural modifications of the corner edge, namely: 1) structure where two hydrogen atoms move apart from each other, yielding relatively large displacement ( $>0.2$  Å) of carbon atoms to which they are attached [Figures 16c and 16f], 2) structure where absence of two hydrogen atoms under the consideration results in a partial reconstruction of the dangling bonds in the corner edge [Figure 16d and 16g], and 3) structure with extra carbon atom, terminated with hydrogen, in the corner [Figures

16e and 16h]. The first corner structure shows a profound signal in the corner, which is reduced in the second structure due to partial break of bipartite symmetry upon reconstruction of dangling bonds. On the other hand, the third structure is characterized by the complete disappearance of the edge-localized states in the corner. A closer examination of spatially decaying behaviour of the edge localized states [Figures 16f-16h] revealed that reduced or vanished LDOS at the inner carbon sites is apparent (see dotted circle in Figure 16h), which is reproduced well in the experiment [Figure 16iii]. To understand the disappearance of the edge-localized states, we examine closer the balance between two sublattices in the corner [Figures 16j and 16k]. It is well known that the edge-localized states originate from the local imbalance between two sublattices at the edges [see Figure 1], which can be seen as larger LDOS at four and three zigzag sites that are aligned linearly along the hole-edges for the models in Figures 16c and 16d, and Figure 16 e, respectively. In contrast to the linearly aligned zigzag-edge sites, the extra carbon site at the corner in the model in Figure 16e is isolated and belongs to the different sublattice compared to the rest of the hole-edge sites (see Figure 16k). Thus the isolated carbon site belonging to A(B) sublattice locally makes a pair with an adjacent hole-edge site belonging B(A) sublattice (see the dotted circle in Figure 16k). The resultant local sublattice symmetry is balanced in a similar manner with that of the armchair edge (see Figure 1). Since the A-B paired armchair edge does not support the edge states, the local pairing of the A-B sublattice explains the disappearance of the edge state at the corner structure in Figures 16iii and 16h.

## Conclusions

Combined scanning probe and first-principles characterisation of a chemically modified graphene nanostructure make it possible to identify the exact chemistry of the graphene edges on the atomic scale and their related electronic activities. The chemistry-dependent electronic properties can be basically understood on the basis of the interplay of edge geometry and chemistry, which induces the modulation of a graphene- $\pi$  electron network, as can be intuitively seen in the corresponding Clar formulas. Depending on the number of hydrogen atoms attached to the linear zigzag edge, the edge-localised  $\pi$ -state with the large densities of states near  $E_F$  (*i.e.*, radical character) switches back and forth, which leads to ON-OFF switching of the electronic activity. The attachment of oxygen atoms at the linear zigzag edges causes the drastic change in the effective boundary conditions of the  $\pi$ -electron network, which induce a quasi-localised edge state with a spatially extended character. In a similar manner as the hydrogenated linear edges, the electronic properties of the hydrogenated vacancy-defects are subject to significant modulation in response to chemical details at the internal defect-edges. The defect-localized  $\pi$ -state at the fully mono-hydrogenated vacancy can be quenched by addition of a hydrogen atom at the defect-internal edge, which inevitably links to the electronic and magnetic activities. We provided experimental evidence of dynamical switching functionality of the edge-localised  $\pi$  state at the oxidised point defects, which is induced by dynamic changes in the bonding configuration of the

oxygen atoms (*i.e.*, ether/carbonyl forms). In addition to the number of foreign chemical species attached to the edge, their bonding configurations have in fact a strong impact on the electronic properties.

This study reveals that precise control of the chemistry at the graphene edge is crucial for understanding the unique defect-localised  $\pi$  state in graphene materials, which could be an important aspect of fabricating future graphene-based electronic devices.

### Figure 1

(a) Graphene honeycomb bipartite lattice structure, where the white and black circles denote A and B sublattice sites, respectively. The unit cell is indicated by a dotted hexagon. The two typical crystallographic directions of the armchair and zigzag directions are indicated by arrows. (b) Chemical structures of infinite graphene, which are described by resonance of three Clar formulas. The sextet consisting of six  $\pi$  electrons is represented by a circle. The unit cell is indicated by the dotted lines. (c) Unique Clar formula of the hydrogenated armchair edge. (d) Clar formulas of the mono-hydrogenated zigzag edge, which are represented by three degenerated formulas. The black dot denotes an unpaired electron. (e) First Brillouin zone of graphene. Reciprocal lattice vectors are denoted by  $\mathbf{a}^*$  and  $\mathbf{b}^*$ .  $\mathbf{K} = 2\pi/a(1/3, 1/\sqrt{3})$ ,  $\mathbf{K}' = 2\pi/a(2/3, 0)$ ,  $\Gamma = (0, 0)$ . (f) Bipartite model of the armchair edge, where open and filled circles denote the A and B sublattice sites, respectively. Secondary carbon sites belonging to A or B sublattice at the boundary are coloured orange. (g) Bipartite model of the zigzag edge. Secondary carbon sites at the boundary are denoted by orange circles. In (c),(d),(f), and (g) the unit cells are denoted by dotted brackets.

### Figure 2

LDA-calculated band structures and graphene nanoribbon models with the (a) armchair edge and (b) zigzag edge. Black and blue balls in the models represent carbon and hydrogen atoms, respectively. The xyz axis is shown at the bottom left corner in each model. In the all figure, DFT calculations were performed in a similar manner as describe in refs [6,27,28] unless otherwise noted.

### Figure 3

(a) Experimental ultrahigh vacuum (UHV)-STM height image of a nanohole with mono-atomic depth prepared by atomic hydrogen etching of the single atomic vacancies in the graphene layer on graphite (imaging conditions:  $V_s = 0.1$  V,  $I = 0.9$  nA, scale bar = 1 nm). Arrows indicate the zigzag directions of the graphene lattice. The nanohole edges are aligned in the zigzag directions. Three types of nanohole edges (b)-(d) are indicated by the dotted lines. (b-g) STM images and local density approximation (LDA) simulations for the mono-hydrogenated zigzag edge (b and c, respectively), the partially di-hydrogenated zigzag edge (d and e, respectively), and the fully di-hydrogenated zigzag edges (f and g, respectively) (imaging conditions:  $V_s = 0.1$  V,  $I = 0.7$  nA, imaging area =  $1.35 \times 1.35$  nm<sup>2</sup>). The images correspond to the edges (b), (c) and (d) indicated in (a). The observed periodicities in the STM images are schematically represented by green circles:  $a \times a$ ,  $\sqrt{3}a \times \sqrt{3}a$ , and  $a \times a$  for (b), (d), and (f),

respectively. The zigzag and armchair directions are indicated by arrows in (d). The di-hydrogenated site is indicated by dotted circles in (e). The hydrogen atom in the C-H participating in hyperconjugation is encircled by a green line in (f). Black and blue balls in the models represent carbon and hydrogen atoms, respectively. The isosurface obtained by integrating local density of states within bias range from 0.1 to 0 V in the simulation and those in Figures 4, 7, 9, 15 and 16 are coloured orange.

#### 10 Figure 4

Experimental UHV-STM height image of the hydrogenated armchair edge and the LDA simulation (imaging conditions:  $V_s = 0.1$  V,  $I = 0.7$  nA, scale bar = 1 nm). The observed  $\sqrt{3}a \times \sqrt{3}a$  periodicity in the STM image is extended into the interior and is schematically represented by green circles. Arrow indicates the armchair direction. Black and blue balls in the models represent carbon and hydrogen atoms, respectively.

#### Figure 5

(a) The two degenerated Clar formulas of the partially di-hydrogenated zigzag edge. (b) The superposition of the sextet positions in the two formulas in (a). (c) The bipartite model of the partially di-hydrogenated edge. The secondary carbon sites at the boundary are denoted by orange circles. (d) The three degenerated Clar formulas of the fully di-hydrogenated edge. The black dot denotes an unpaired electron. (e) The bipartite model of the fully di-hydrogenated edge. The primary carbon sites at the bearded boundary are denoted by orange circles. (f) One of the Clar formulas of the fully di-hydrogenated edge where the  $\text{CH}_2$  moiety is involved in a hyperconjugation interaction with the bulk graphene  $\pi$ -electron network. The unit cells are denoted by dotted brackets.

#### Figure 6

LDA-calculated band structures and graphene nanoribbon models with (a) the partially di-hydrogenated zigzag edge, (b) the fully di-hydrogenated zigzag edge, and (c) the carboxylated zigzag edge. The LDA approximation was used for (a) and (b) and the PBE0 approximation was used for (c).<sup>26</sup> Black, red, and blue balls in the models represent carbon, oxygen, and hydrogen atoms, respectively. The xyz axis is shown at the bottom left corner in each model.

#### Figure 7

(a) Experimental ambient STM height image of the graphite surface after 10 cycles of a potential sweep from 1.0 to 1.9 V at 20 mV  $\text{s}^{-1}$  in a 0.1 M  $\text{H}_2\text{SO}_4$  solution at room temperature (imaging conditions:  $V_s = 0.8$  V,  $I = 0.4$  nA, scale bar = 50 nm). (b) High-resolution STM-current image of an oxidised zigzag edge of the nanographene fragment with an atomically sharp zigzag edge boundary. The edge-localised state represents large amplitudes on one of the graphene sublattice sites with  $a \times a$  periodicity ( $a = 0.24$  nm) that decay into the interior from the edge boundary. The arrow indicates the zigzag direction of the graphene lattice (imaging conditions:  $V_s = 0.2$  V, scale bar = 0.5 nm). (c) PBE0 simulation for the carboxylated zigzag edge, in which the  $a \times a$  periodicity is superimposed. Black and red balls represent carbon and oxygen atoms, respectively. The hybrid

PBE0 calculations were performed using Quantum Espresso code with norm-conserving pseudopotentials and a wave function cutoff energy of 40 Ry. The Brillouin zone integration was performed using a uniform  $4 \times 4 \times 1$  Monkhorst-type k-point grid. (d) LDA-based free energy of the oxidised zigzag graphene nanoribbon models terminated by carboxyl, alcohol, and ether groups versus the electrochemical potential, which are denoted by red, blue, and green lines, respectively.

#### Figure 8

(a) Three degenerated Clar formulas and (b) bipartite model of the carboxylated zigzag edge. The black dot denotes an unpaired electron in (a). Primary carbon sites at bearded oxygen sites at the boundary are denoted by red circles in (b). The unit cells are denoted by dotted brackets.

#### 75 Figure 9

(a) Experimental UHV-STM height image showing a non-passivated mono-atomic vacancy in the topmost graphite layer with three-fold symmetry (imaging conditions:  $V_s = 0.1$  V,  $I = 0.4$  nA, imaging area:  $2.2 \times 2.2$  nm<sup>2</sup>). (b)-(e) UHV-STM height images ((b), (c)) and LDA simulations ((d), (e)), respectively, for the two main types of hydrogenated vacancies with and without the vacancy-internal-edge-localised state, where the three edge sites are mono-hydrogenated in the former, while one of the edge sites is di-hydrogenated with others being mono-hydrogenated in the latter. The three vacancy-internal-edge sites with higher local densities of states are marked by green circles in (b) and (d) (imaging conditions:  $V_s = 0.1$  V,  $I = 0.4$  nA). The mono-hydrogenated vacancy in (d) is characterized by an  $a \times a$  periodic pattern ( $a$ : lattice constant (0.246 nm) on one of the graphene-sublattice-sites, while the partially di-hydrogenated vacancy in (e) does not indicated such periodic pattern. Black and blue balls represent carbon and hydrogen atoms, respectively.

#### Figure 10

(a) Possible hydrogenated vacancy structures obtained by geometrical optimisation of mono-atomic vacancies with 1–6 hydrogen atoms in a graphene supercell ( $8a \times 8a$ ,  $a$  = graphene lattice constant). The initial atomic configurations were generated with the hydrogen atoms on the top and/or bottom of the vacancy-internal edge sites. The atomic positions were then relaxed to the closest local minimum of the LDA total energy. The notation of  $V(n_1, n_2, n_3)$  represents the chemical compositions of the hydrogenated mono-atomic vacancies. The indices  $n_1$ ,  $n_2$ , and  $n_3$  denote the number of hydrogen atoms attached to each of three vacancy's undercoordinated carbon sites. Black and blue balls in the models represent carbon and hydrogen atoms, respectively. (b) Free energy of the hydrogenated vacancy,  $G_H$ , versus chemical potential,  $\mu_H$ , of the atomic hydrogen gas phase for the models in (a). The potential window is estimated from partial pressure of the atomic hydrogen gas and the temperature range of 800–1000°C which corresponds to the experimentally measured temperatures ( $900 \pm 100^\circ\text{C}$ ) during the sample preparation process.

#### 115 Figure 11

(a), (b) LDA-calculated band structures and graphene supercell

models of the energetically favourable hydrogenated vacancies V(111) and V(211), respectively (see the caption in Figure 10). Here we used a relatively small graphene supercell ( $4a \times 4a$ ,  $a =$  graphene lattice constant), which indicates that basic physics (*i.e.*, the emergence and disappearance of the flat band, the charge density distribution pattern of the low-energy  $\pi$  state, and the optimised geometries of the hydrogenated vacancy structures) is almost unchanged regardless of the cell sizes. For band structures of larger graphene supercell calculations ( $8a \times 8a$ ,  $a =$  graphene lattice constant), see ref. [28]. The flat band in (a) is indicated by an arrow. Black and blue balls in the models represent carbon and hydrogen atoms, respectively. (c) and (d) The bipartite models for V(111) and V(211), respectively. The  $\text{CH}_2$  site in (d) has no free  $p_z$  orbital and thus is regarded as a vacancy. The white and black circles denote A and B sublattice sites, respectively. (e),(f) Spin-GGA-calculated band structures of V(111) for graphene supercells ( $4a \times 4a$  (e) and  $9a \times 9a$  (f),  $a =$  graphene lattice constant). The blue circles and red triangles denote bands of  $\alpha$ -spin and  $\beta$ -spin states, respectively. The black line is a band for paramagnetic state. The Dirac point is located at the K point in the Brillouin zone (BZ) in (e). The dotted line is for eyes to indicate band points at the K point. In (f), the Dirac point is at the  $\Gamma$  point, which is due to the BZ folding.

### Figure 12

(a) Current mapping image of the reduced-oxidised graphene on Au(111), where oxidised vacancy defects exhibit a vacancy-internal-edge-localised state, as indicated by the dotted circles. The defect exhibited reversible ON-OFF switching during the repeated imaging. (b) One of the switching events of the defect in (a). During the imaging from top to bottom, the vacancy-internal-edge-localised state switched from ON to OFF. The switching position is indicated by the dotted line (imaging conditions:  $V_s = 2$  mV). The low-energy charge density patterns around the vacancy defects for the ON and OFF states are characterised by the  $a \times a$  and  $\sqrt{3}a \times \sqrt{3}a$  periodicities, respectively, which are schematically superimposed on the image.

### Figure 13

Pairs of oxidised vacancy models with the reversible switching of the vacancy-internal-edge-localised state. The ON state was characterised by quasi-flat band(s) crossing the Fermi level, whereas the OFF states did not exhibit such flat bands in the LDA-calculated band structures (not shown here). Rectangular graphene supercells containing 72 carbon atoms ( $1.476 \times 1.278$  nm) were used for the calculations. The activation barriers for the ON-to-OFF/OFF-to-ON transitions were 0.2/2.5 eV and 0.8/0.7 eV for Models 1 and 2, respectively. The smaller activation barrier (0.2 eV) for the ON-to-OFF transition in Model 1 was not substantially enough to separate the two states at room temperature.

### Figure 14

(a) Top perspective of the two configurations of the ON and OFF states in Model 2 (Figure 13) with and without an edge-localised  $\pi$  state. (b) Bipartite models for ON and OFF states. The carbonyl group has a free  $p_z$  orbital and thus is regarded as an additional A sublattice site, which is represented by a red circle. The white and

black circles denote A and B sublattice sites, respectively.

### Figure 15

(a) LDA-calculated band structures of ON and OFF states. The flat band of the ON state is indicated by an arrow. (b) LDA simulations of the ON and OFF states, which reproduce the  $a \times a$  and  $\sqrt{3}a \times \sqrt{3}a$  periodicities around the defect and the ON-OFF switching of the vacancy-internal edge. A graphene supercell ( $9a \times 9a$ ,  $a =$  graphene lattice constant) was used for the calculations.

### Figure 16

(a),(b) Representative STM images of nanoholes with atomically smooth boundaries. Images size  $6 \times 6$  nm<sup>2</sup>. Imaging conditions:  $V_s = 0.35$  V,  $I = 0.3$  nA. In (a), arrows indicate the zigzag directions of the graphene lattice. (i)-(iii) Zoomed-up images of 150°- (i), 120°- (ii), and 60°- (iii) corner edges. The position of (i)-(iii) are represented by dotted circles in (a) and (b). STM cross sectional profiles along the green solid line in (ii) and (iii) are shown in insets. (c)-(e) LDA-calculated LDOS isosurfaces for three possible structures of the 60° corner edge (see the text for details). (f)-(h) Zoomed-up images of the isosurface at the corners of (c)-(e), respectively, in which inner carbon sites with higher LDOS are marked by red circles, while carbon sites with reduced or vanished LDOS (*i.e.*, node sites) are indicated by dotted circles. Black and blue balls represent carbon and hydrogen atoms, respectively. DFT calculations are performed in a similar manner as described in ref. [6]. (j) Bipartite models for (c) and (d). (k) Bipartite models for (e). The dotted circle in (k) is one example of a local pairing of A(B) and B(A) sublattice at the edge sites. Secondary carbon sites at the hole-edges are denoted by orange circles. The white and black circles denote A and B sublattice sites, respectively.

### Acknowledgements

This work was supported by Grants-in-Aid for Scientific Research (No. 20001006, No. 23750150, and No. 25790002) from the Ministry of Education, Culture, Sports, Science and Technology of Japan.

### Notes and references

- <sup>1</sup> <sup>a</sup> Department of Chemistry, Tokyo Institute of Technology, 2-12-1 Ookayama, Meguro-ku, Tokyo 152-8551, Japan.  
<sup>2</sup> <sup>b</sup> Department of Organic and Polymeric Materials, Tokyo Institute of Technology, Ookayama, Meguro-ku, Tokyo 152-8552, Japan.  
<sup>3</sup> <sup>c</sup> Graduate School of Engineering Science, Osaka University, 1-3 Machikaneyama-cho, Toyonaka, Osaka 560-8531, Japan

<sup>†</sup> Authors with equal contributions

<sup>‡</sup> On the basis of a simple valence bond theory, the electronic state around the partially hydrogenated edge could be represented by superposition of the three resonant structures (states). It should be noted here that, for more precise discussion, we have to consider weighting of each of the three states in the superposition depending on the eigenvalue of each state if available

<sup>§</sup> In the hydrolysis process, which involves oxygen evolution (*i.e.*,  $2\text{H}_2\text{O} \rightarrow \text{O}_2 + 4\text{H}^+ + 4\text{e}^-$ ), the effective local pressure (concentration) of the oxygen molecules at the graphene-liquid interface is as high as  $10^2$  Pa, which could accelerate the oxidation process.

- 1 M. Fujita, K. Wakabayashi, K. Nakada and K. Kusakabe, Peculiar localized state at zigzag graphite edge *J. Phys. Soc. Jpn.*, 1996, **65**, 1920-1923.
- 2 K. Nakada, M. Fujita, G. Dresselhaus and M. S. Dresselhaus, Edge state in graphene ribbons: nanometer size effect and edge shape dependence *Phys. Rev. B*, 1996, **54**, 17954-17961.
- 3 S. E. Stein and R. L. Brown,  $\pi$ -Electron properties of large condensed polyaromatic hydrocarbons *J. Am. Chem. Soc.*, 1987, **109**, 3721-3729.
- 4 Y. Kobayashi, K. Fukui, T. Enoki, K. Kusakabe and Y. Kaburagi, Observation of zigzag and armchair edges of graphite using scanning tunneling microscopy and spectroscopy *Phys. Rev. B*, 2005, **71**, 193406.
- 5 Y. Niimi, T. Matsui, H. Kambara, K. Tagami, M. Tsukada and H. Fukuyama, Scanning tunneling microscopy and spectroscopy studies of graphite edges *Appl. Surf. Sci.*, 2005, **241**, 43-48.
- 6 M. Ziatdinov, S. Fujii, K. Kusakabe, M. Kiguchi, T. Mori and T. Enoki, Visualization of Electronic States on Atomically Smooth Graphitic Edges with Different Types of Hydrogen Termination *Phys. Rev. B*, 2013, **87**, 115427.
- 7 H. Yang, A. J. Mayne, M. Boucherit, G. Comtet, G. Dujardin and Y. Kuk, Quantum Interference Channeling at Graphene Edges *Nano Lett.*, 2010, **10**, 943-947.
- 8 C. Park, H. Yang, A. J. Mayne, G. Dujardin, S. Seo, Y. Kuk, J. Ihm and G. Kim, Formation of Unconventional Standing Waves at Graphene Edges by Valley Mixing and Pseudospin Rotation *Proc. Natl. Acad. Sci. U. S. A.*, 2011, **108**, 18622-18625.
- 9 K. Sakai, K. Takai, K. Fukui, T. Nakanishi and T. Enoki, Honeycomb superperiodic pattern and its fine structure near the armchair edge of graphene observed by low-temperature scanning tunneling microscopy *Phys. Rev. B*, 2010, **81**, 235417.
- 10 C. N. R. Rao, A. K. Sood, K. S. Subrahmanyam and A. Govindaraj, Graphene: The New Two-Dimensional Nanomaterial *Angew. Chem., Int. Ed.*, 2009, **48**, 7752-7777.
- 11 O. V. Yazyev, Emergence of Magnetism in Graphene Materials and Nanostructures *Rep. Prog. Phys.*, 2010, **73**, 056501.
- 12 X. Jia, J. Campos-Delgado, M. Terrones, V. Meunier and M. S. Dresselhaus, Graphene Edges: A Review of Their Fabrication and Characterization *Nanoscale*, 2011, **3**, 86-95.
- 13 T. Enoki, Role of Edges in the Electronic and Magnetic Structures of Nanographene *Phys. Scr.*, 2012, **146**, 014008-1-14.
- 14 K. P. Loh, Q. Bao, P. K. Ang and J. Yang, The Chemistry of Graphene *J. Mater. Chem.*, 2010, **20**, 2277-2289.
- 15 L. Chen, Y. Hernandez, X. Feng and K. Müllen, From Nanographene and Graphene Nanoribbons to Graphene Sheets: Chemical Synthesis *Angew. Chem. Int. Ed.*, 2012, **51**, 7640-7654.
- 16 J. M. Carlsson, F. Hanke, S. Linic and M. Scheffler, Two-Step Mechanism for Low-Temperature Oxidation of Vacancies in Graphene *Phys. Rev. Lett.*, 2009, **102**, 166104.
- 17 A. A. El-Barbary, R. H. Telling, C. P. Ewels, M. I. Heggie and P. R. Briddon, Structure and energetics of the vacancy in graphite *Phys. Rev. B*, 2003, **68**, 144107.
- 18 P. O. Lehtinen, A. S. Foster, Yuchen Ma, A.V. Krasheninnikov and R. M. Nieminen, Irradiation-Induced Magnetism in Graphite: A Density Functional Study *Phys. Rev. Lett.*, 2004, **93**, 187202.
- 19 L. R. Radovic and B. Bockrath, On the Chemical Nature of Graphene Edges: Origin of Stability and Potential for Magnetism in Carbon Materials *J. Am. Chem. Soc.*, 2005, **127**, 5917-5927.
- 20 T. Wassmann, A. P. Seitsonen, A. M. Saitta, M. Lazzeri and F. Mauri, Structure, Stability, Edge States, and Aromaticity of Graphene Ribbons *Phys. Rev. Lett.*, 2008, **101**, 096402.
- 21 H. Zheng and W. Duley, First-Principles Study of Edge Chemical Modifications in Graphene Nanodots *Phys. Rev. B*, 2009, **78**, 045421.
- 22 G. Lee and K. Cho, Electronic Structures of Zigzag Graphene Nanoribbons with Edge Hydrogenation and Oxidation *Phys. Rev. B*, 2009, **79**, 165440.
- 23 A. P. Seitsonen, A. M. Saitta, T. Wassmann, M. Lazzeri and F. Mauri, Structure and Stability of Graphene Nanoribbons in Oxygen, Carbon Dioxide, Water, and Ammonia *Phys. Rev. B*, 2010, **82**, 115425.
- 24 T. Wassmann, A. P. Seitsonen, A. M. Saitta, M. Lazzeri and F. Mauri, Clar's Theory,  $\pi$ -Electron Distribution, and Geometry of Graphene Nanoribbons *J. Am. Chem. Soc.*, 2010, **132**, 3440-3451.
- 25 X. Zhang, O. V. Yazyev, J. Feng, L. Xie, C. Tao, Y.-C. Chen, L. Jiao, Z. Pedramrazi, A. Zettl, S. G. Louie et al., Experimentally Engineering the Edge Termination of Graphene Nanoribbons *ACS Nano*, 2013, **7**, 198-202.
- 26 M. Ohtsuka, S. Fujii, M. Kiguchi and T. Enoki, Electronic State of Oxidized Nanographene Edge with Atomically Sharp Zigzag Boundaries *ACS Nano*, 2013, **7**, 6868-6874.
- 27 S. Fujii and T. Enoki, Rearrangement of  $\pi$ -Electron Network and Switching of Edge-Localized  $\pi$  State in Reduced Graphene Oxide *ACS Nano*, 2013, **7**, 11190-11199.
- 28 M. Ziatdinov, S. Fujii, K. Kusakabe, M. Kiguchi, T. Mori and T. Enoki, Direct imaging of monovacancy-hydrogen complexes in a single graphitic layer *Phys. Rev. B*, 2014, **89**, 155405.
- 29 L. Talirz, H. Söde, J. Cai, P. Ruffieux, S. Blankenburg, R. Jafaar, R. Berger, X. Feng, K. Müllen, D. Passerone, et al., Termini of Bottom-Up Fabricated Graphene Nanoribbons *J. Am. Chem. Soc.*, 2013, **135**, 2060-2063.
- 30 H. Huang, D. Wei, J. Sun, S. L. Wong, Y. P. Feng, A. H. C. Neto and A. T. S. Wee, Spatially Resolved Electronic Structures of Atomically Precise Armchair Graphene Nanoribbons *Sci. Rep.*, 2013, **2**, 983.
- 31 S. Fujii and T. Enoki, Nanographene and Graphene Edges: Electronic Structure and Nanofabrication *Acc. Chem. Res.*, 2013, **46**, 2202-2210.
- 32 E. Clar, *The Aromatic Sextet*; Wiley: London, 1972.
- 33 C. Tao, L. Jiao, O. V. Yazyev, Y.-C. Chen, J. Feng, X. Zhang, R. B. Capaz, J. M. Tour, A. Zettl, S. G. Louie et al., Spatially Resolving Edge States of Chiral Graphene Nanoribbons *Nat. Phys.*, 2011, **7**, 616-620.
- 34 M. Pan, E. C. Girao, X. Jia, X.; S. Bhaviripudi, Q. Li, J. Kong, V. Meunier and M. S. Dresselhaus, Topographic and Spectroscopic Characterization of Electronic Edge States in CVD Grown Graphene Nanoribbons *Nano Lett.*, 2012, **12**, 1928-1933.
- 35 D. J. Klein, Graphitic Polymer Strips with Edge States *Chem. Phys. Lett.*, 1994, **217**, 261-265.
- 36 K. Kusakabe and M. Maruyama, Magnetic Nanographite *Phys. Rev. B*, 2003, **67**, 092406.
- 37 Y. Li, Z. Zhou, C. R. Cabrera and Z. Chen, Preserving the Edge Magnetism of Zigzag Graphene Nanoribbons by Ethylene Termination: Insight by Clar's Rule *Sci. Rep.*, 2013, **3**, 2030.
- 38 Y.-W. Son, N. Park, S. Han and J. Yu, Magnetic Ordering at the Edges of Graphitic Fragments: Magnetic Tail Interactions between the Edge-Localized States *Phys. Rev. B*, 2005, **72**, 174431.
- 39 E. H. Lieb, Two theorems on the Hubbard model *Phys. Rev. Lett.*, 1989, **62**, 1201.
- 40 P. Giannozzi et al. QUANTUM ESPRESSO: a modular and open-source software project for quantum simulations of materials *J. Phys.: Condens. Matter*, 2009, **21**, 395502.
- 41 J. M. Soler, E. Artacho, J. D. Gale, A. García, J. Junquera, P. Ordejón, and D. Sánchez-Portal, The SIESTA method for ab initio order-N materials simulation *J. Phys.: Condens. Matter*, 2002, **14**, 2745.
- 42 J. P. Perdew, K. Burke, and M. Ernzerhof, *Phys. Rev. Lett.*, 1996, **77**, 3865.
- 43 H. J. Monkhorst and J. D. Pack, *Phys. Rev. B*, 1976, **13**, 518.
- 44 J.-H. Chen, L. Li, W. G. Cullen, E. D. Williams and M. S. Fuhrer, Tunable Kondo effect in graphene with defects *Nature Physics*, 2011, **7**, 535-538.
- 45 A. Kitaev, Periodic table for topological insulators and superconductors *AIP Conf. Proc.*, 2009, **1134**, 22-30, arXiv:0901.2686[cond-mat.mes-hall].
- 46 M. Vanević, V. M. Stojanović, and M. Kindermann, Character of electronic states in graphene antidot lattices: Flat bands and spatial localization *Phys. Rev. B*, 2009, **80**, 045410.
- 47 Y. Shimomura, Y. Takane and K. Wakabayashi, Electronic States and Local Density of States in Graphene with a Corner Edge Structure *J. Phys. Soc. Jap.*, 2011, **80**, 054710.
- 48 P. E. Blochl, Projector augmented-wave method *Phys Rev B* 1994, **50**, 17953.

- 
- 49 J. Tersoff, D. R. Hamann, Theory and Application for the Scanning Tunneling Microscope *Phys. Rev. Lett.*, 1983, **50**, 1998–2001.
- 50 J. Tersoff, D. R. Hamann, Theory of the Scanning Tunneling Microscope *Phys. Rev. B*, 1985, **31**, 805–813.
- s 51 N. T. Cuong, M. Otani, and S. Okada, Absence of edge states near the 120° corners of zigzag graphene nanoribbons *Phys. Rev. B*, 2013, **87**, 045424.

Figure 1a

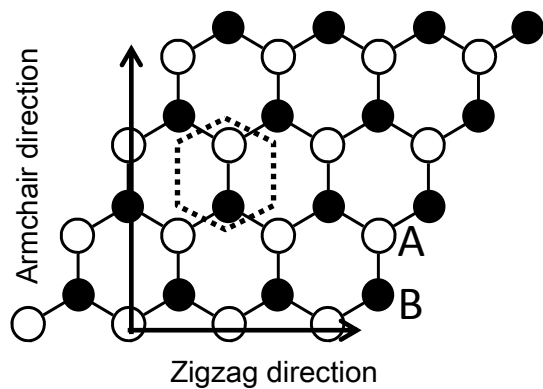


Figure 1b

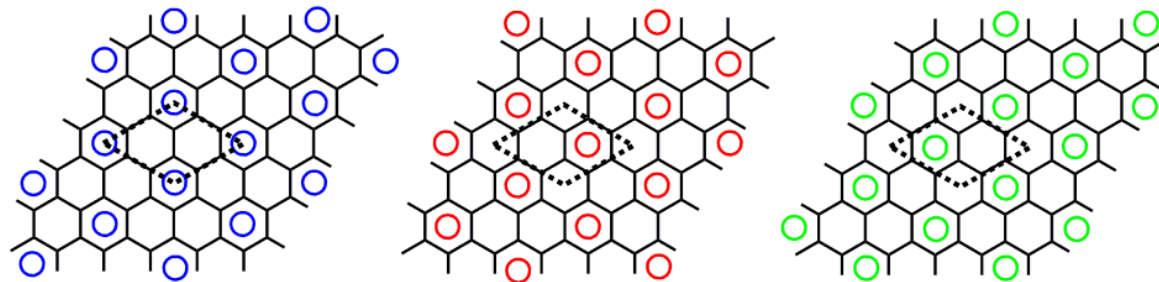


Figure 1c

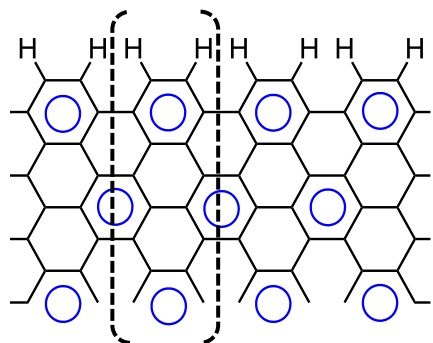


Figure 1e

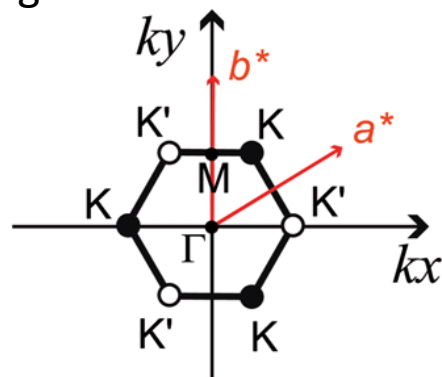


Figure 1f

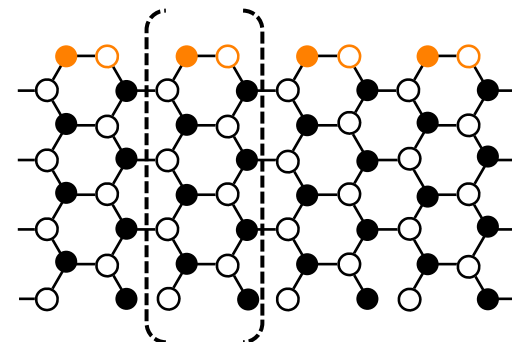


Figure 1d

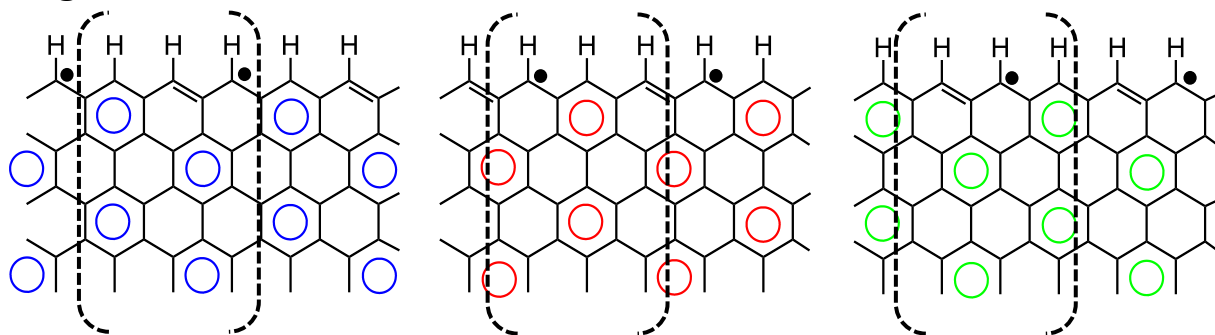
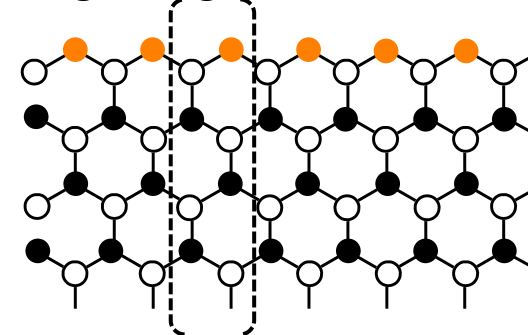


Figure 1g



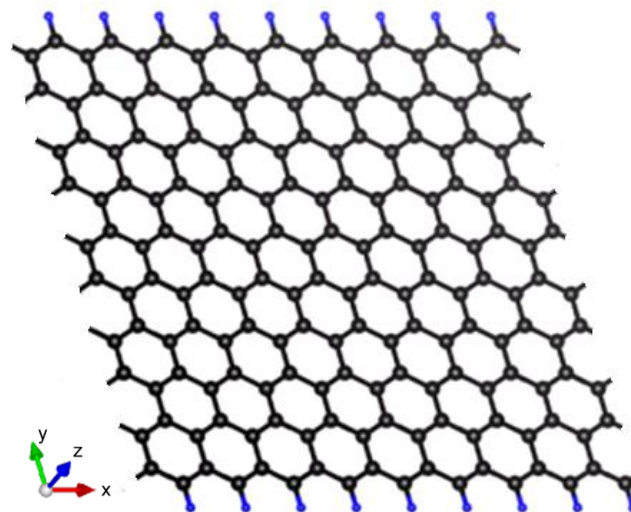
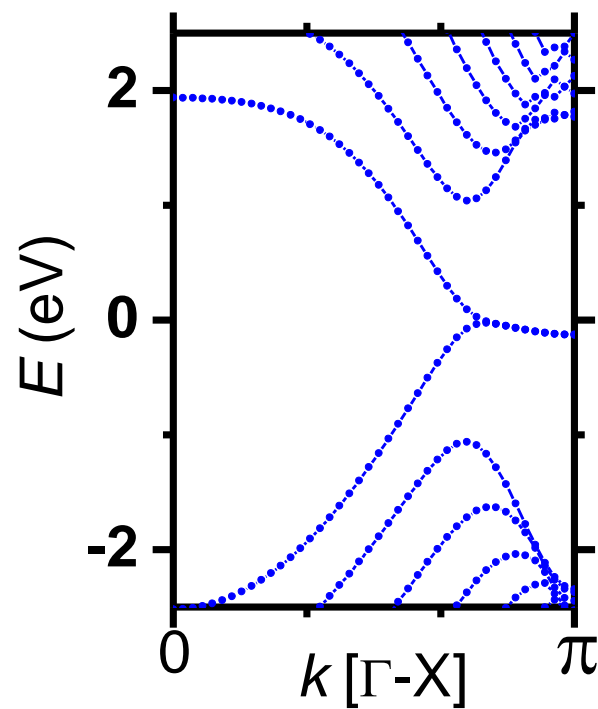
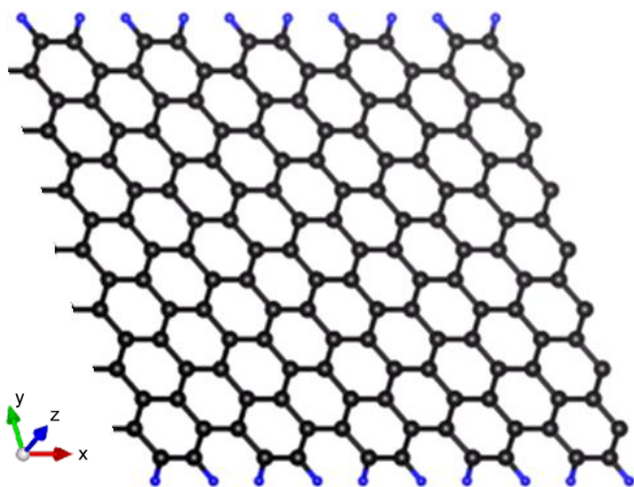
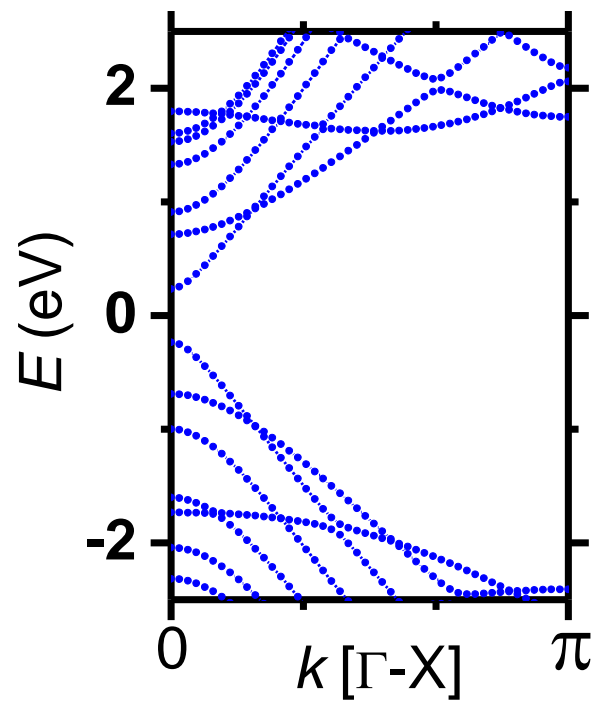


Figure 3a

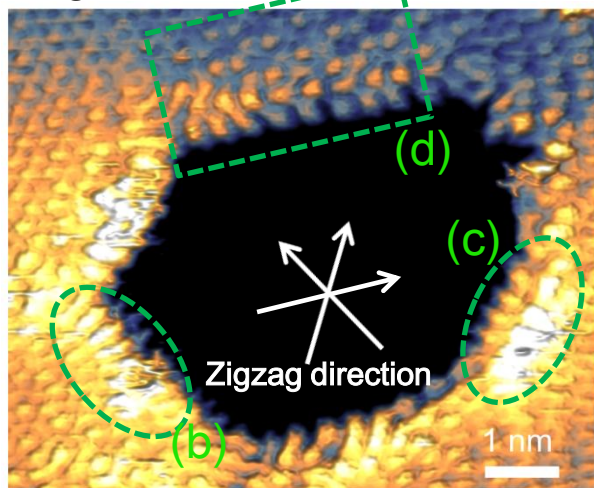


Figure 3b

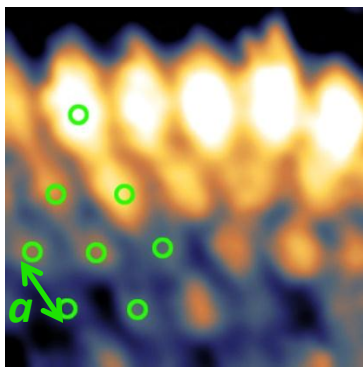


Figure 3c

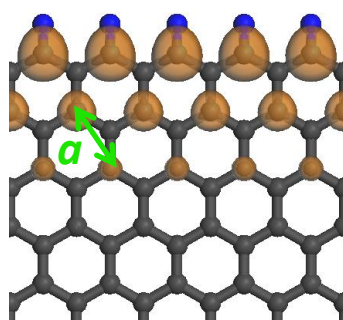


Figure 3d

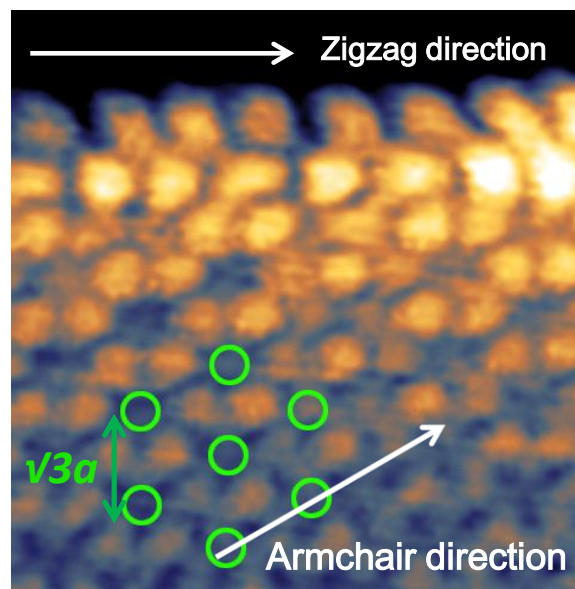


Figure 3e

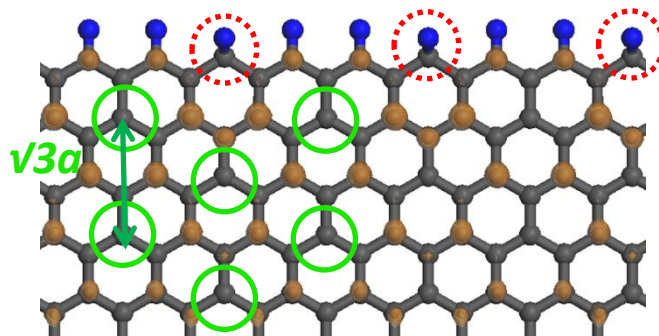


Figure 3f

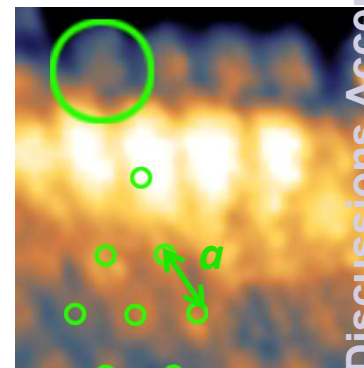


Figure 3g

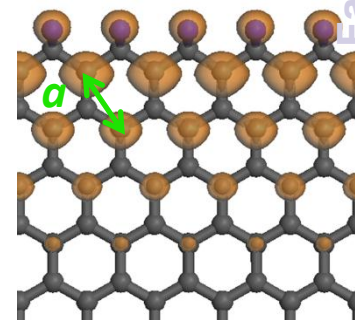


Figure 4a

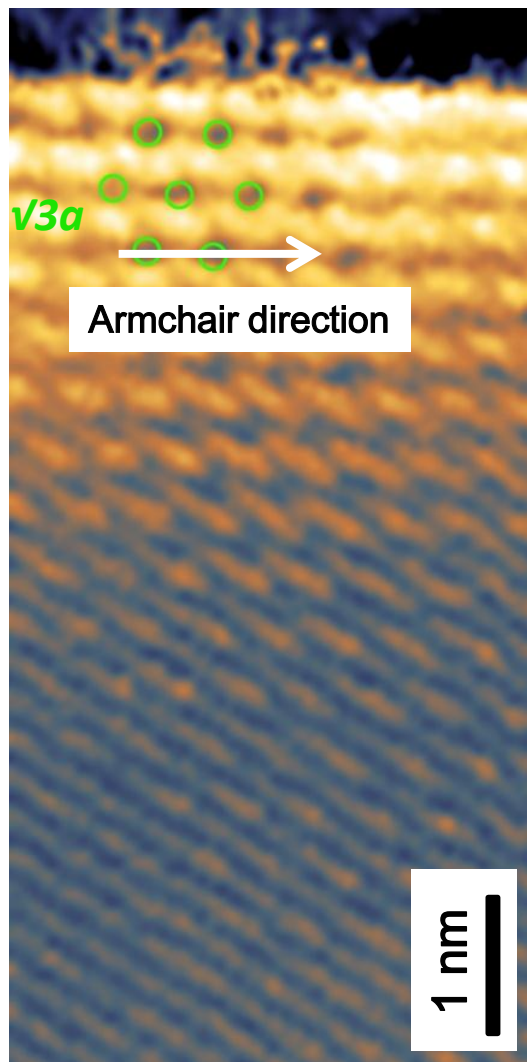


Figure 4b

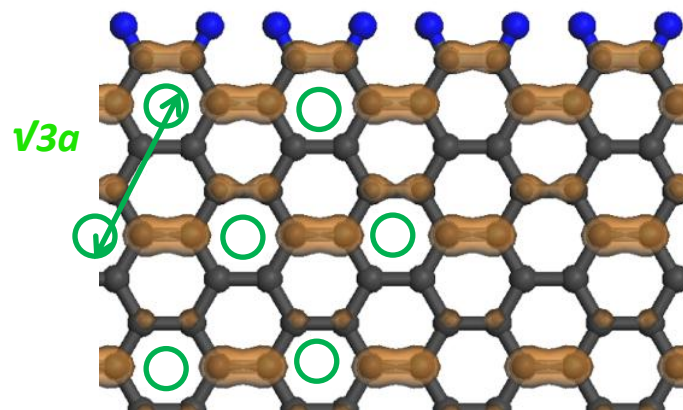


Figure 5a

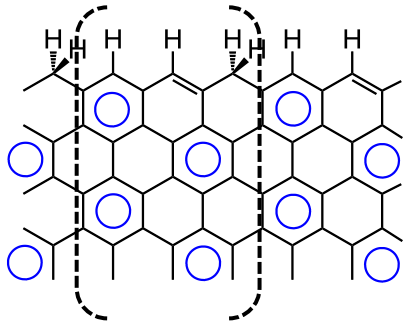


Figure 5b

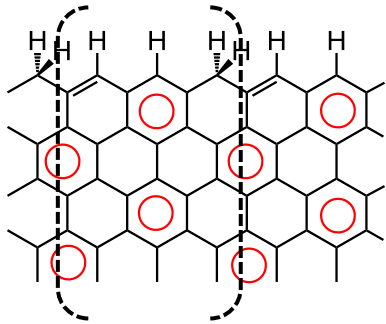


Figure 5c

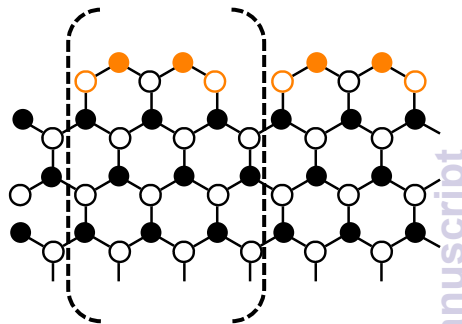


Figure 5d

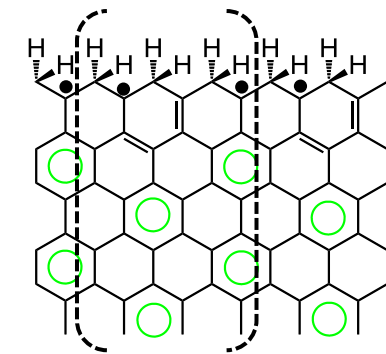
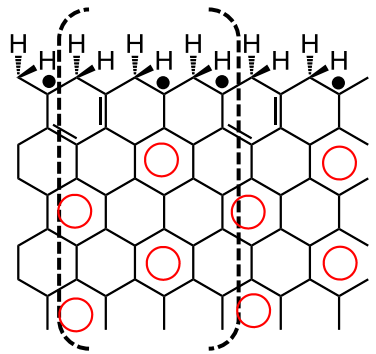
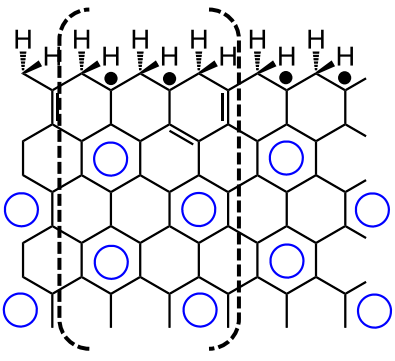


Figure 5e

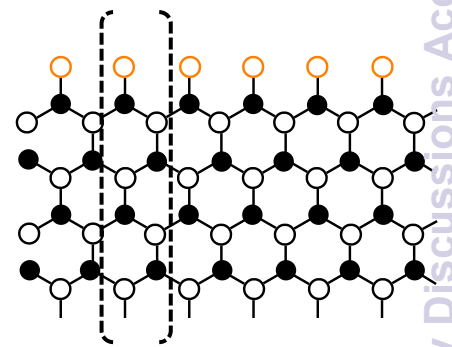


Figure 5f

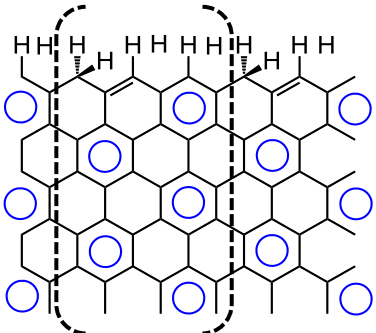


Figure 6a

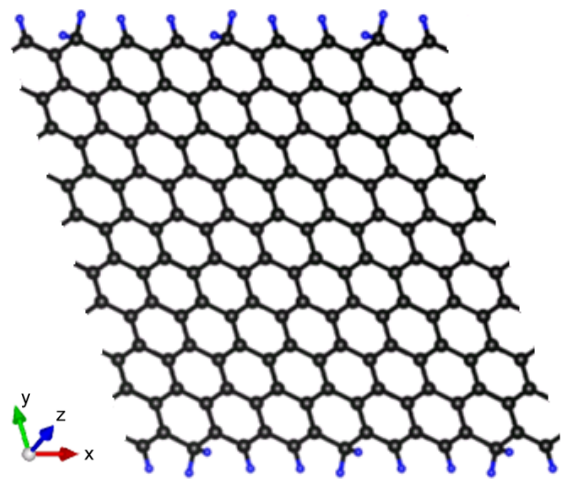
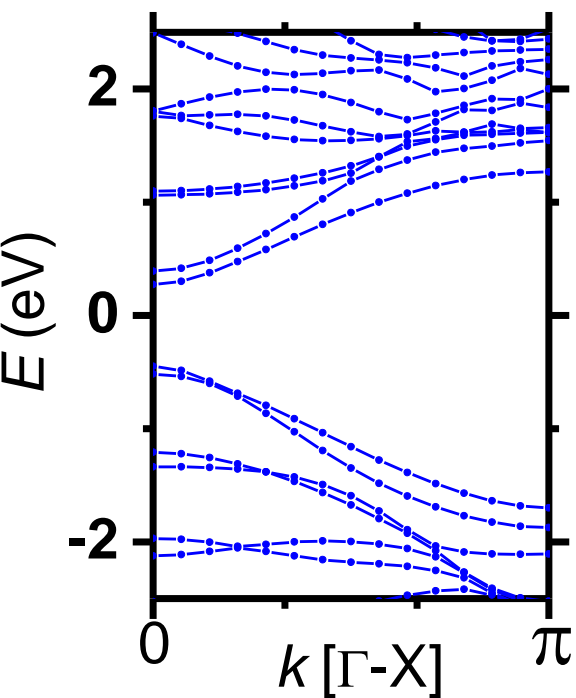


Figure 6b

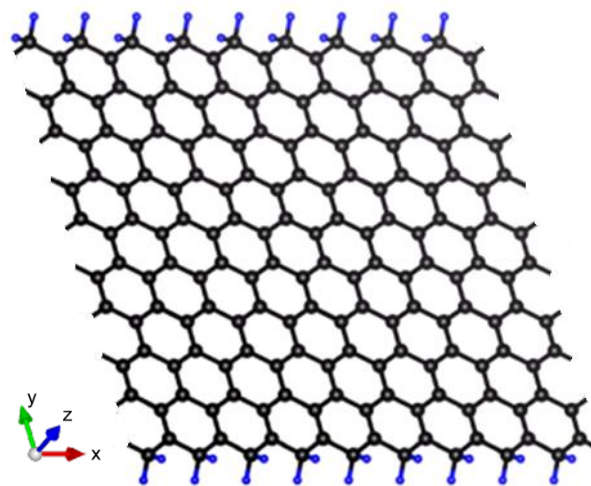
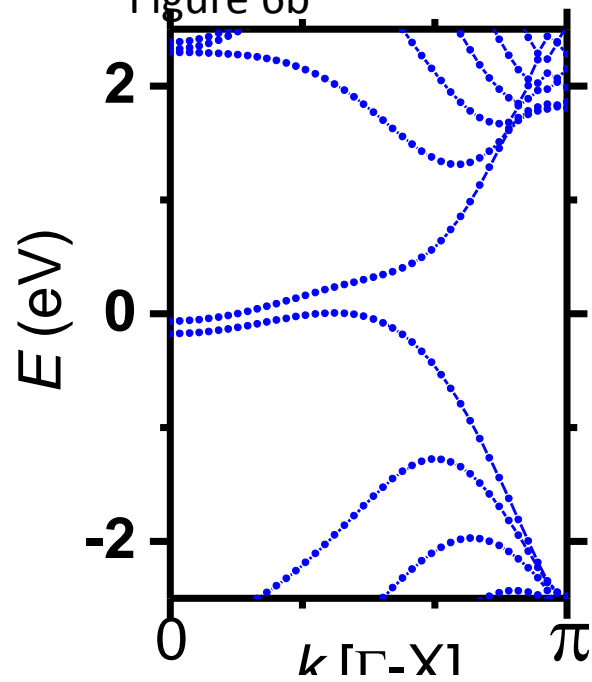


Figure 6c

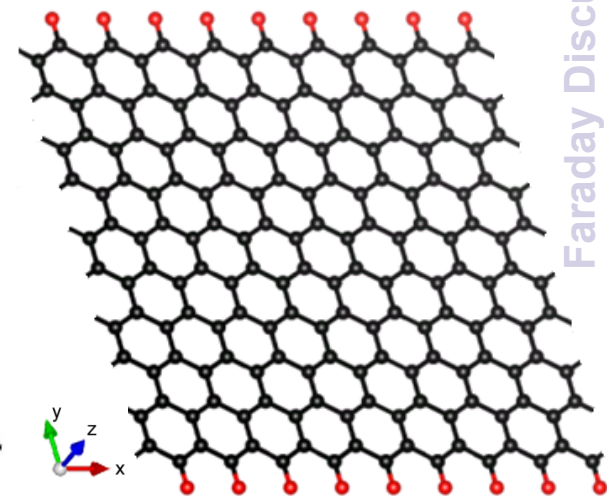
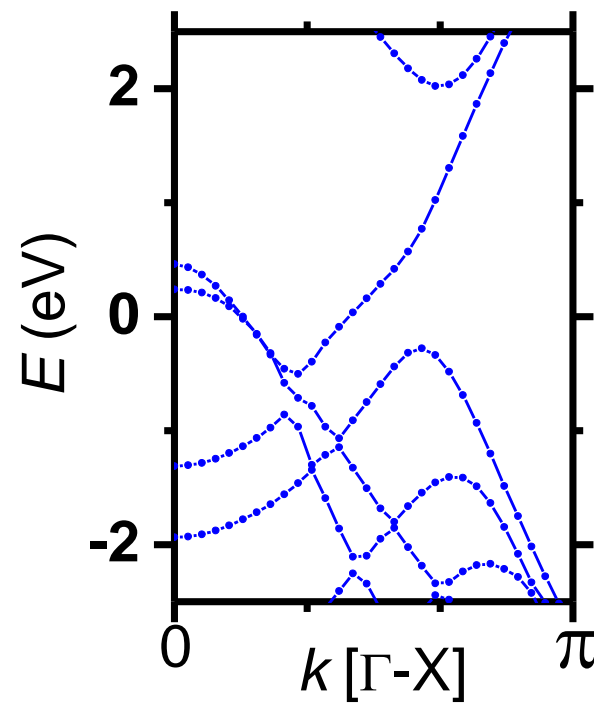


Figure 7a

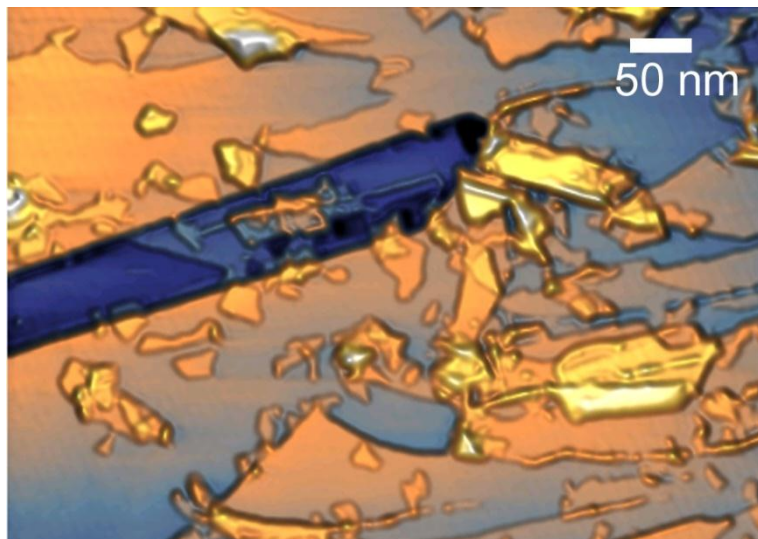


Figure 7b

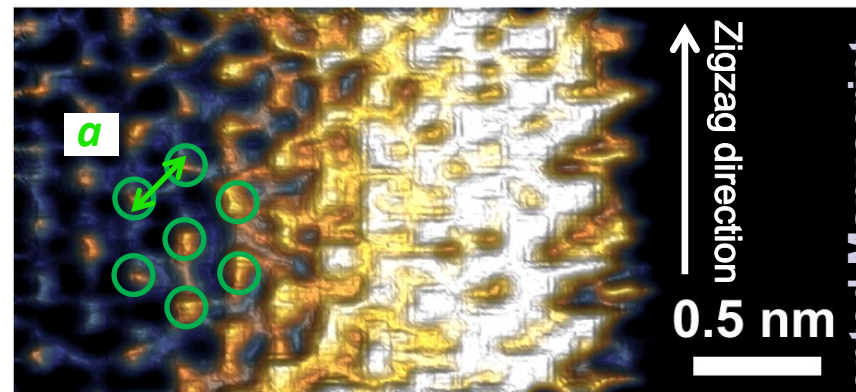


Figure 7c

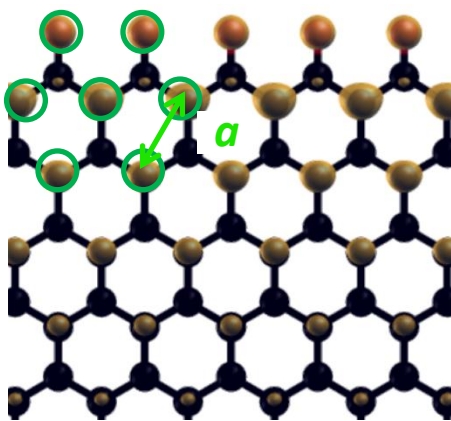


Figure 7d

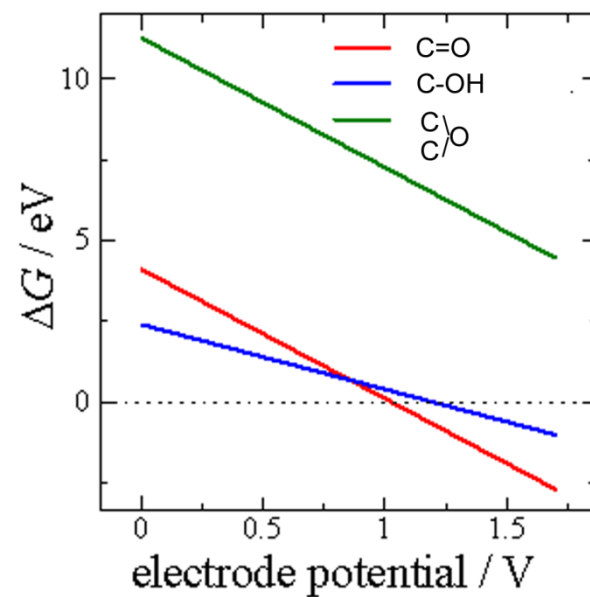


Figure 8a

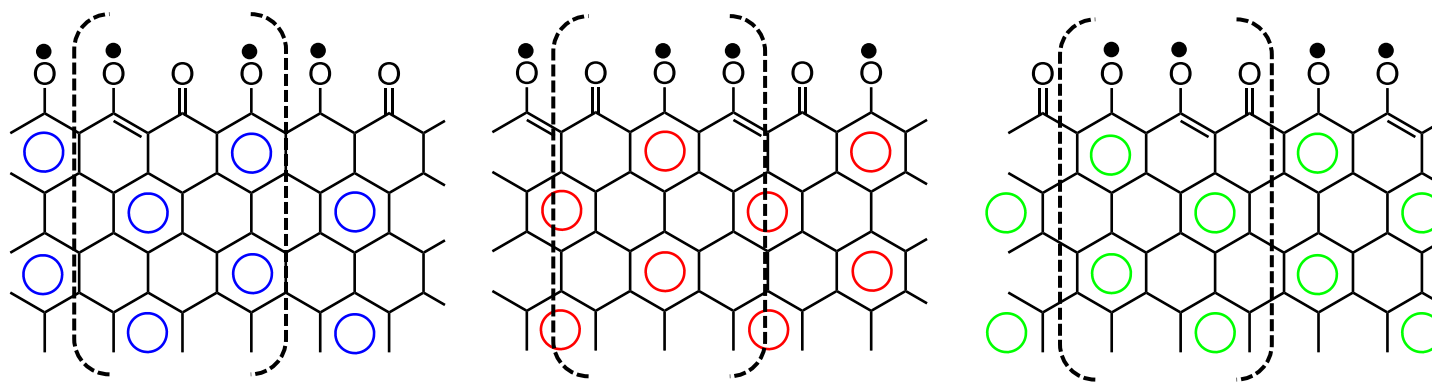


Figure 8b

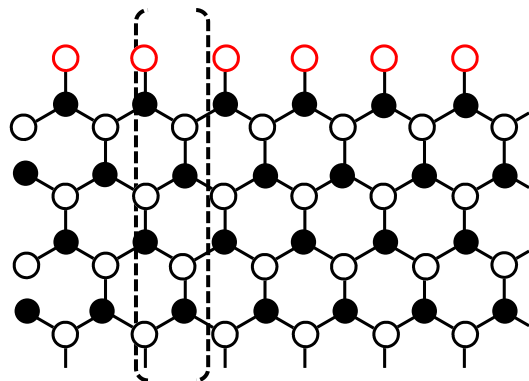


Figure 9a

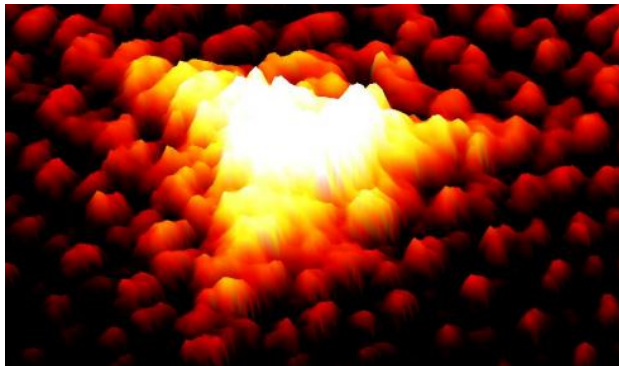


Figure 9b

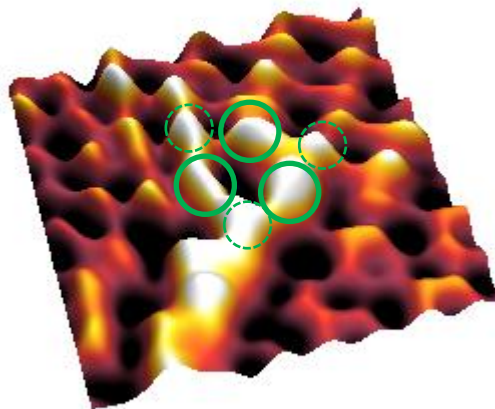


Figure 9c

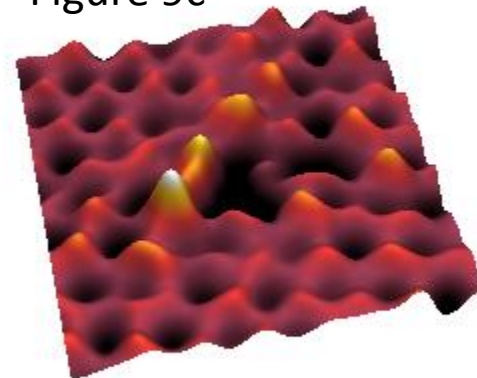


Figure 9d

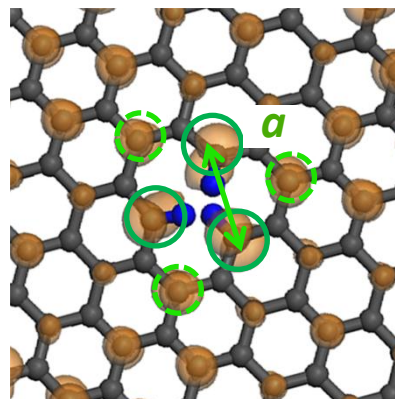


Figure 9e

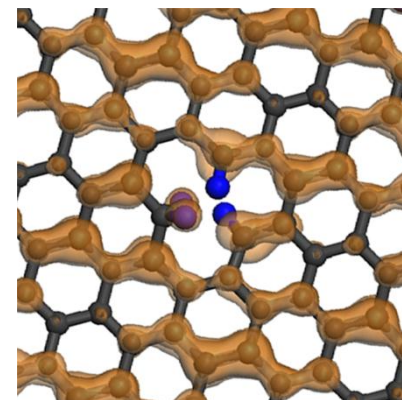


Figure 10a

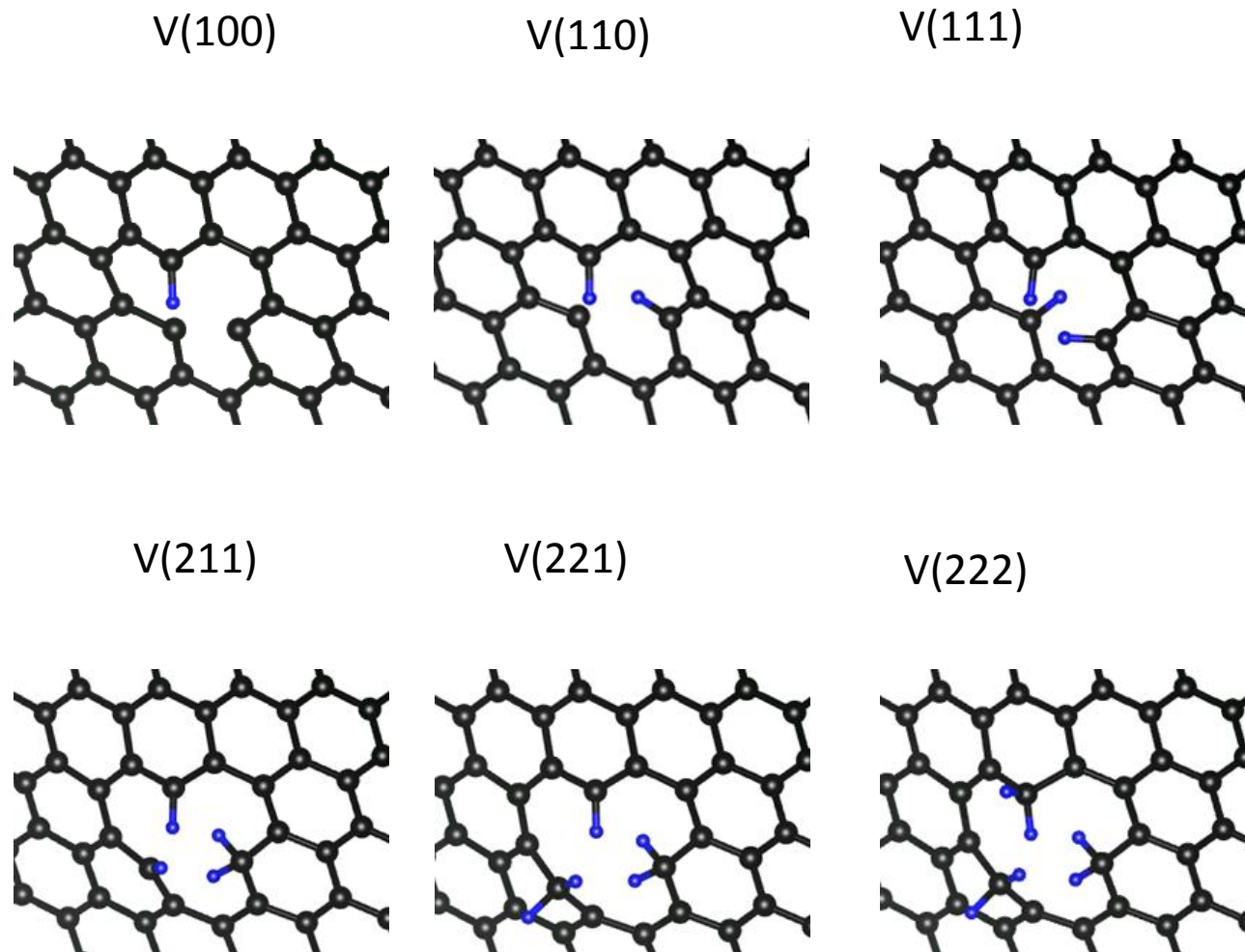


Figure 10b

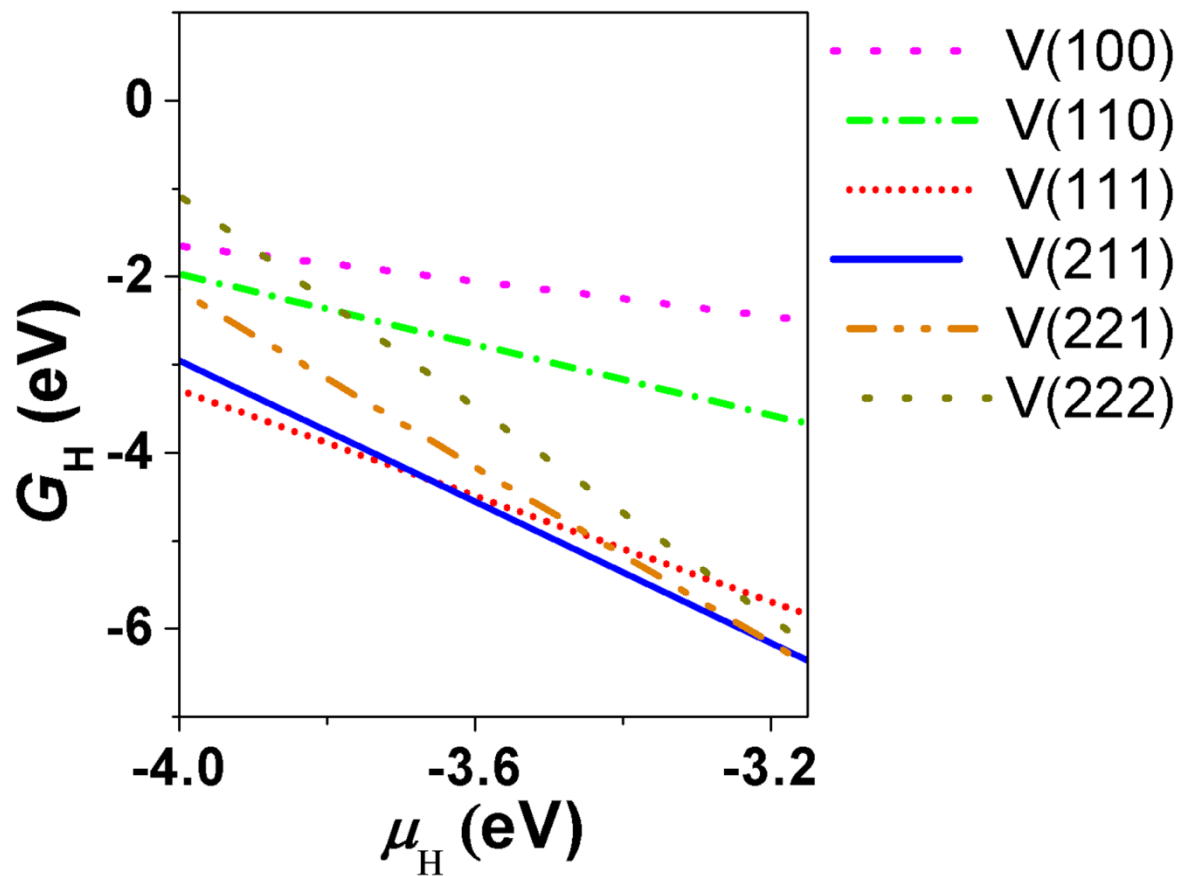


Figure 11a

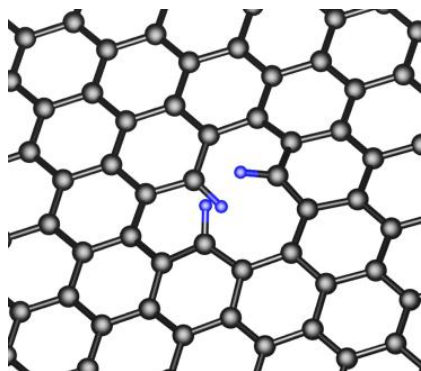
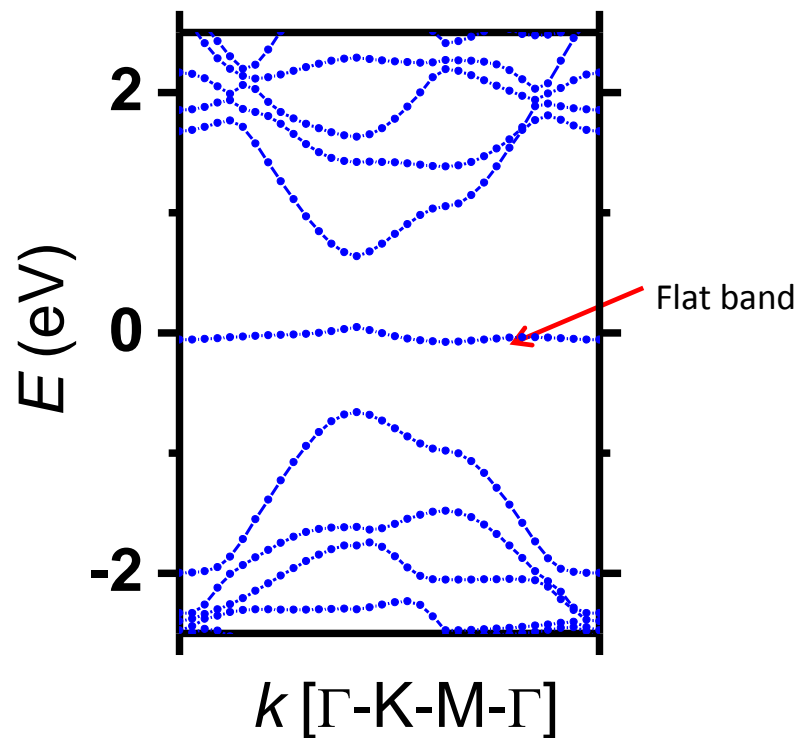


Figure 11b

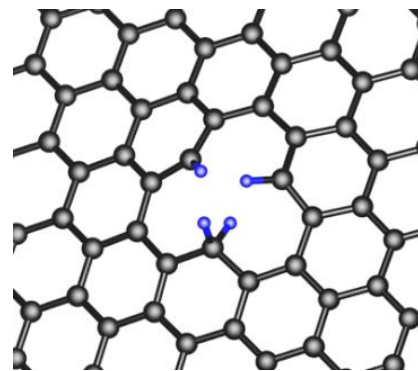
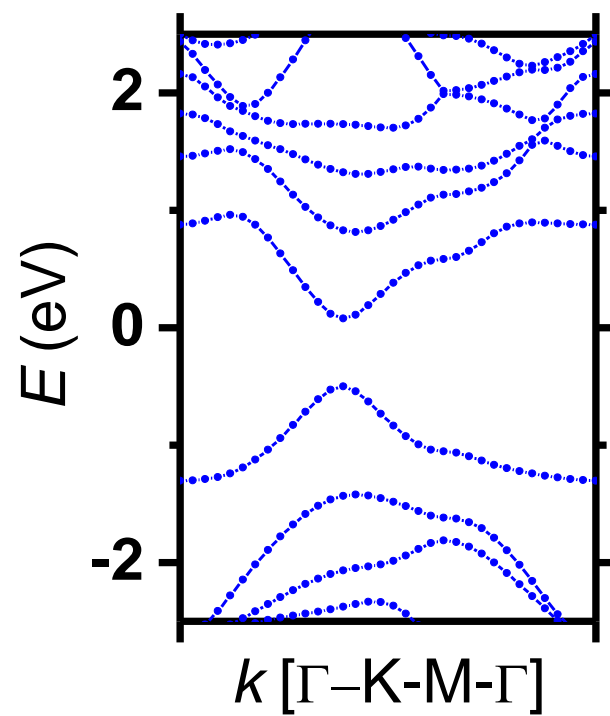


Figure 11c

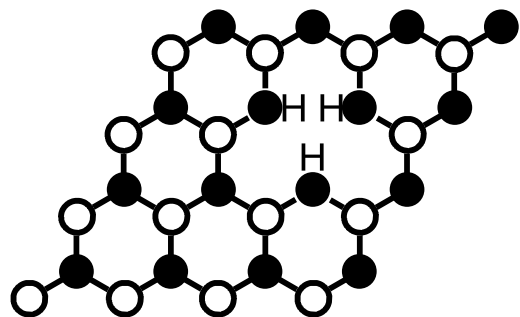


Figure 11d

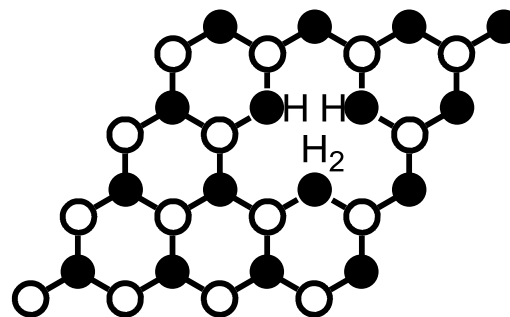


Figure 11e

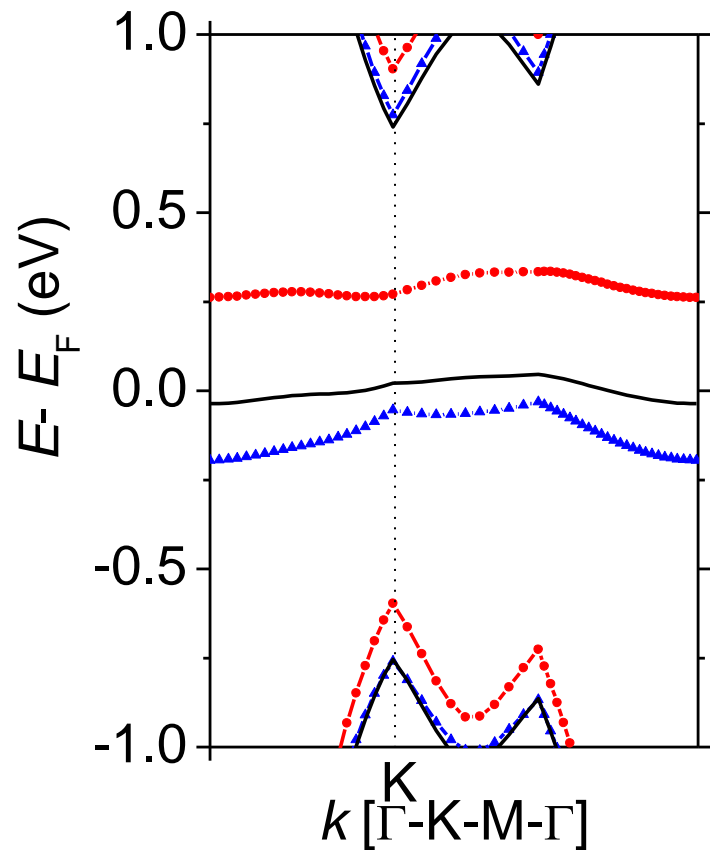


Figure 11f

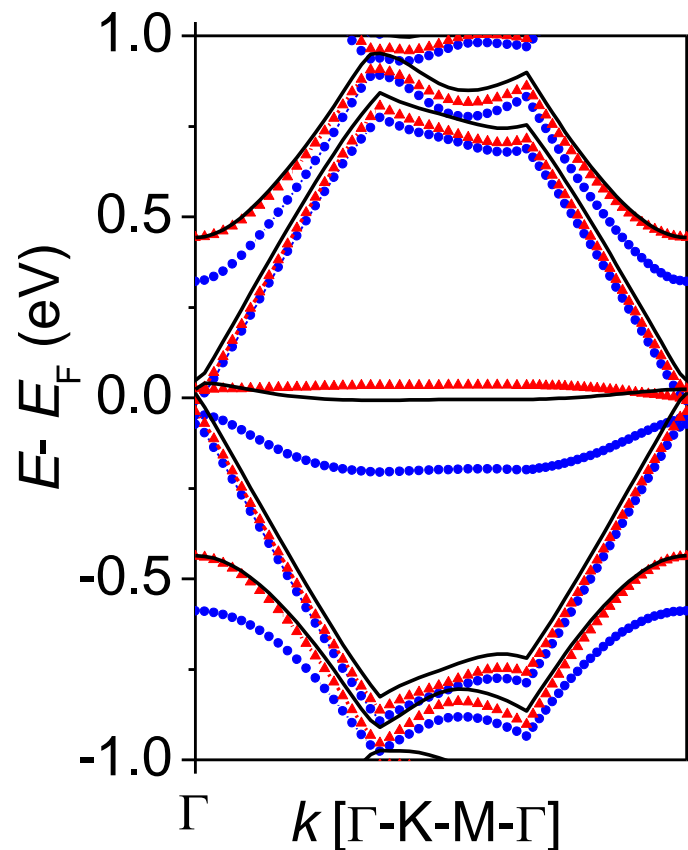


Figure 12a

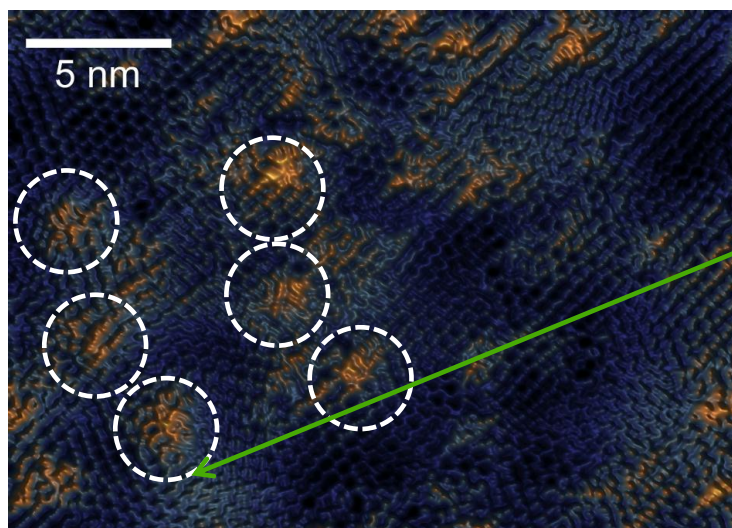


Figure 12b

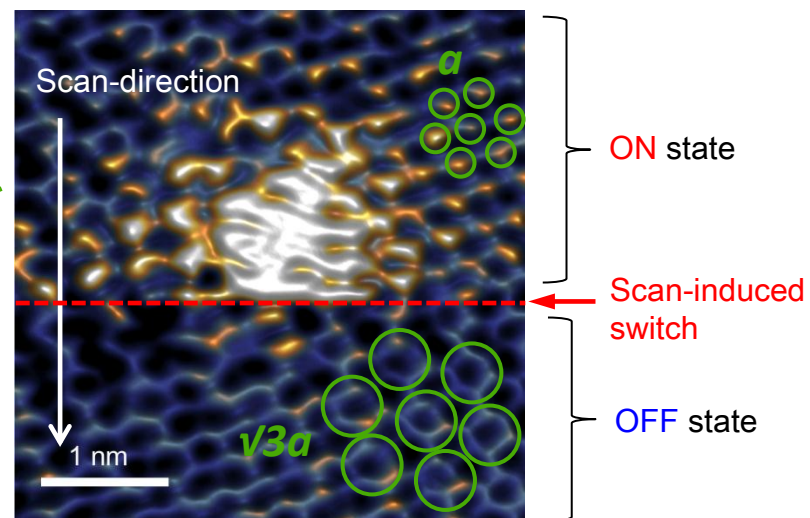


Figure 13

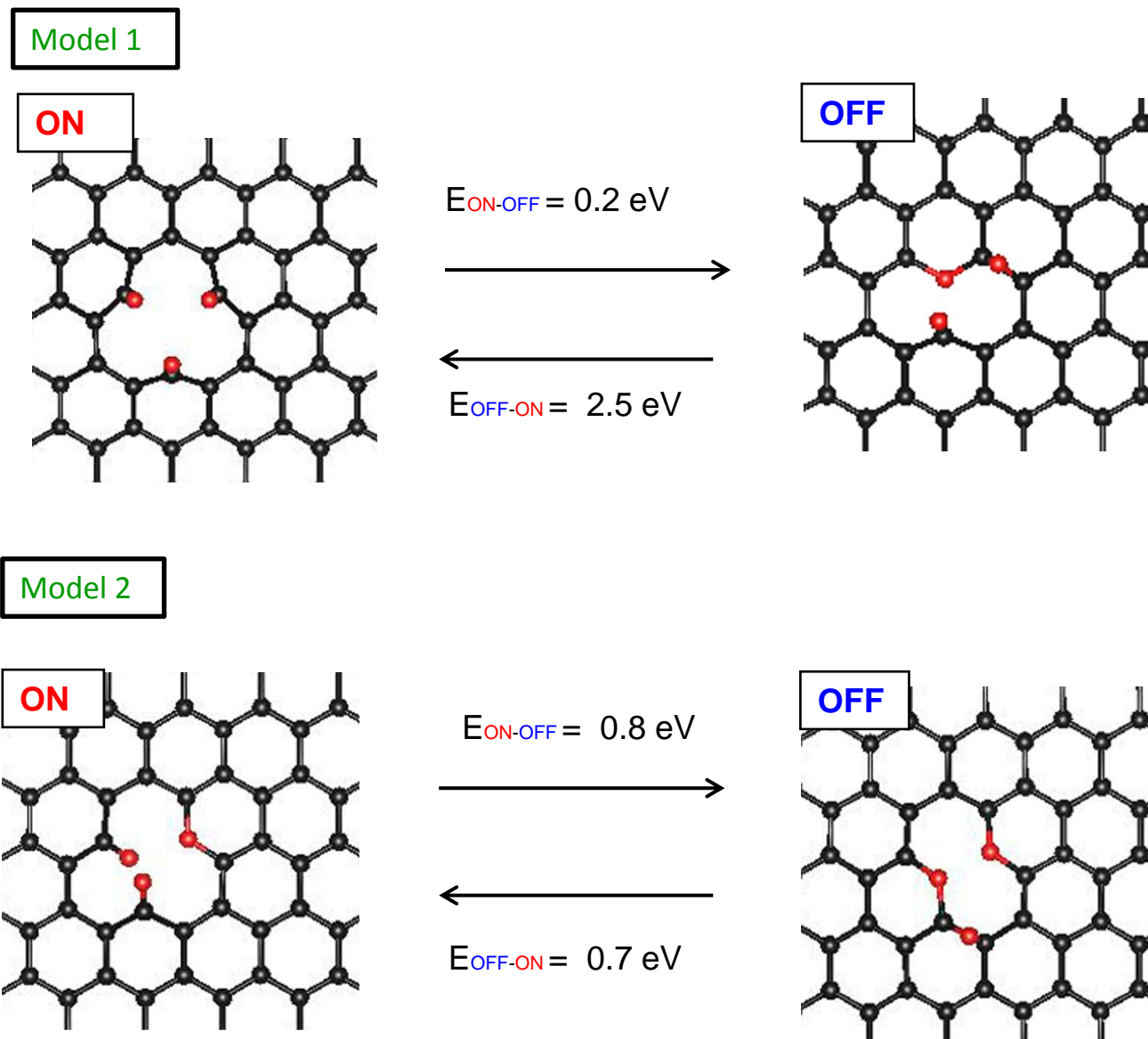


Figure 14a

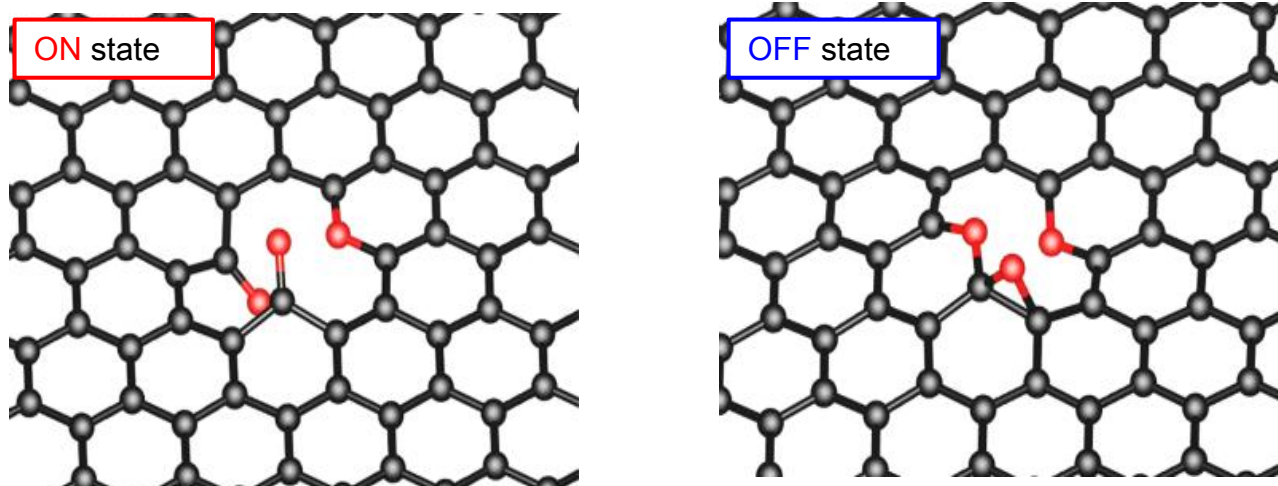


Figure 14b

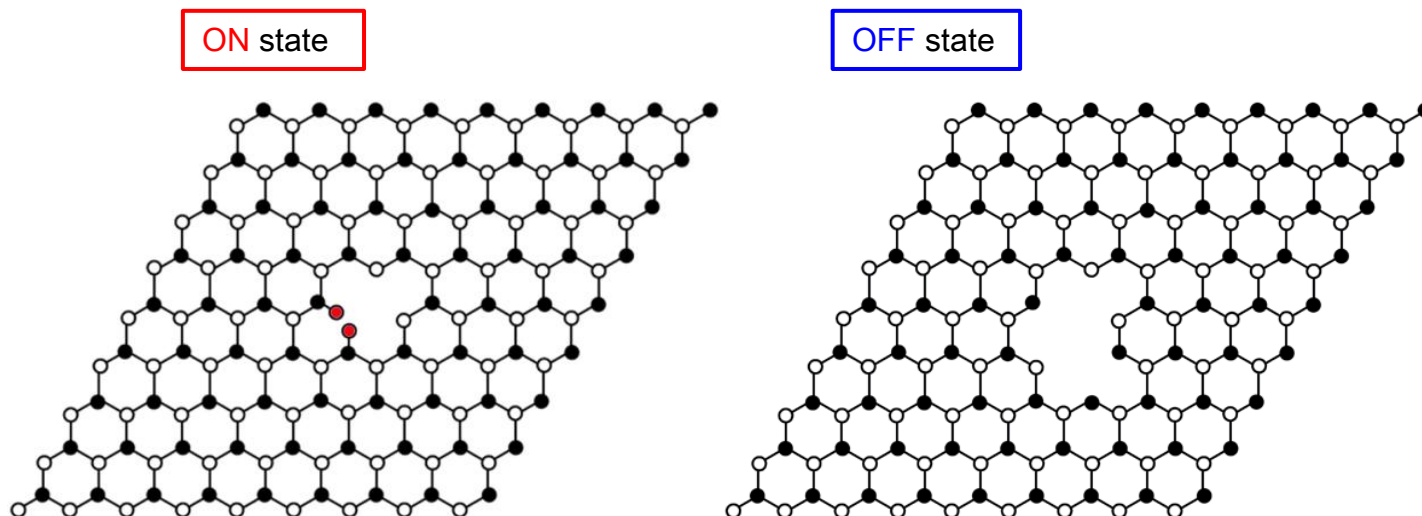


Figure 15a

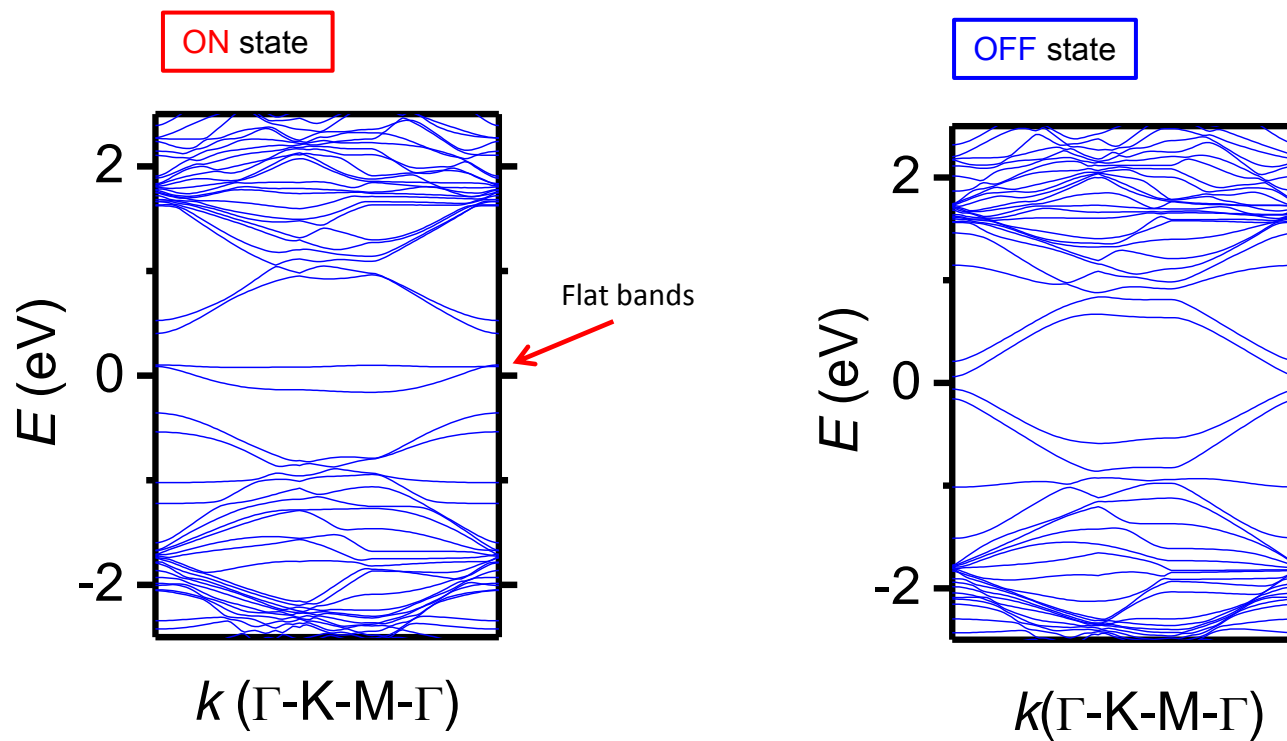


Figure 15b

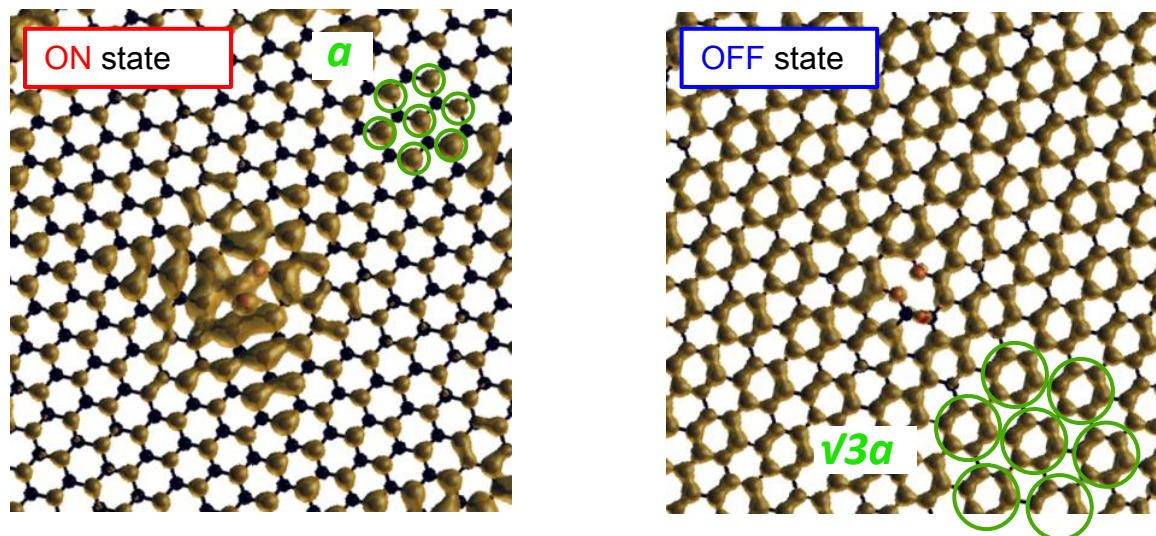
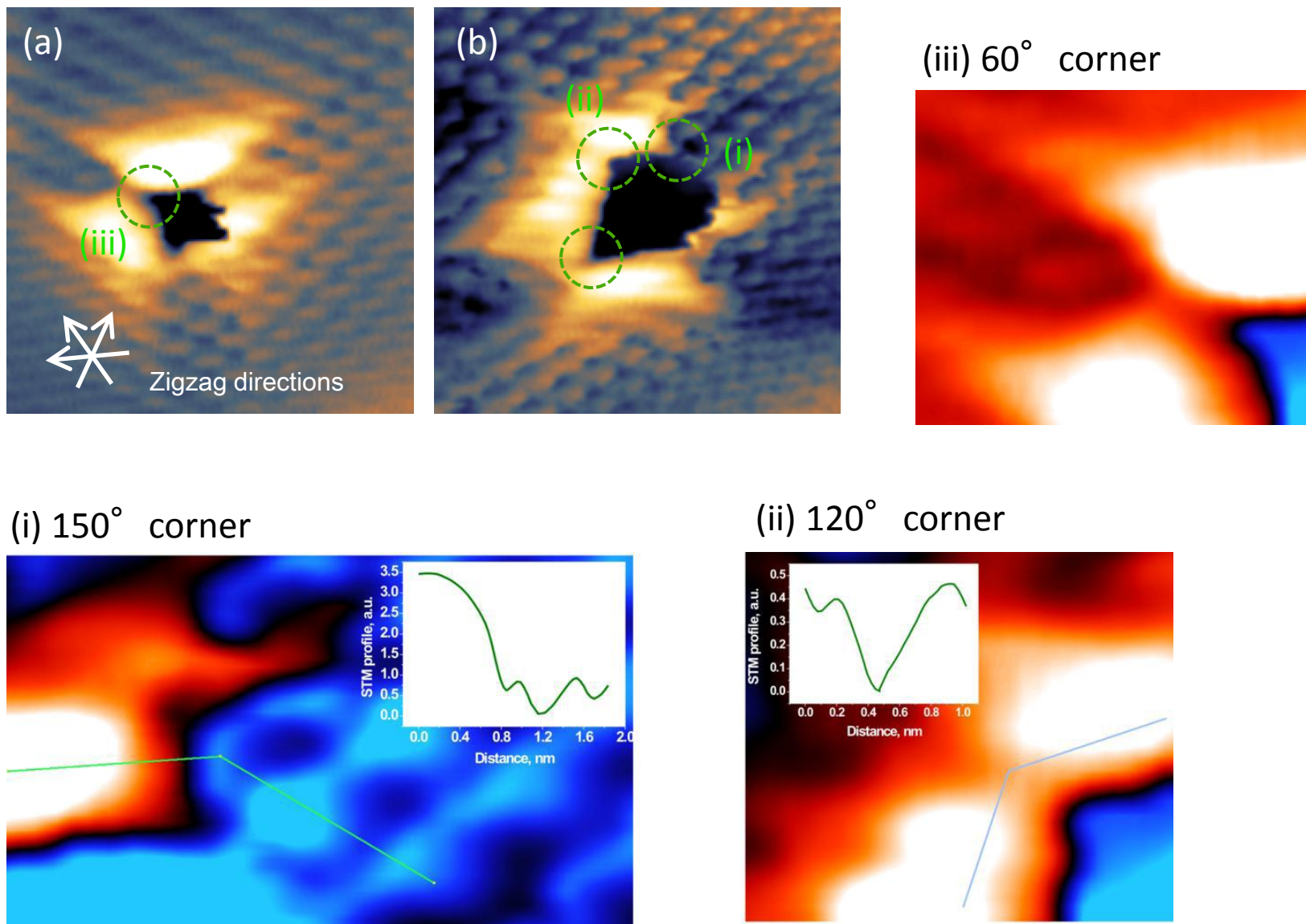
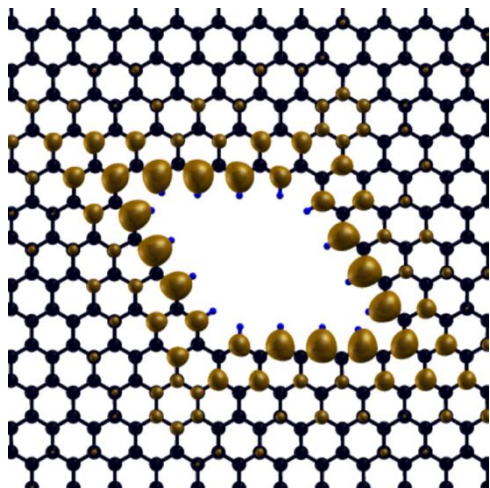


Figure 16

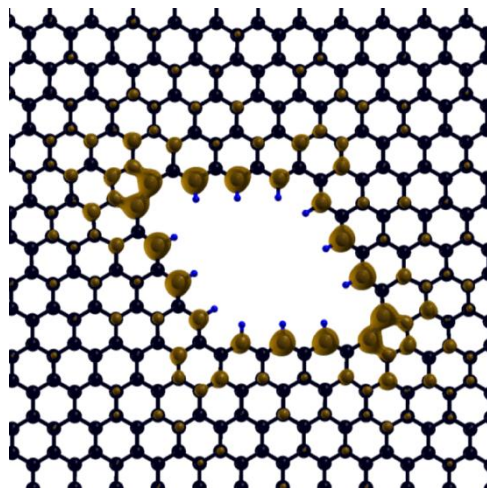


(c)



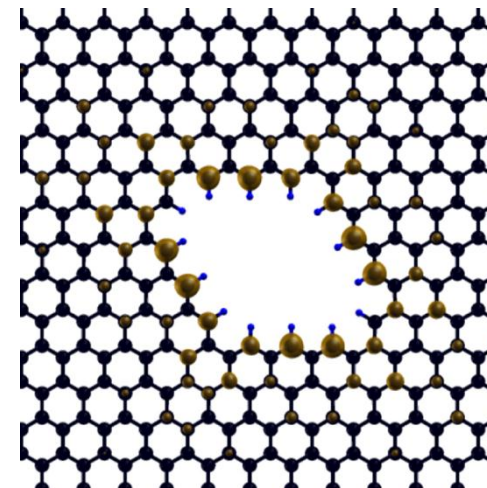
(d)

Faraday Discussions

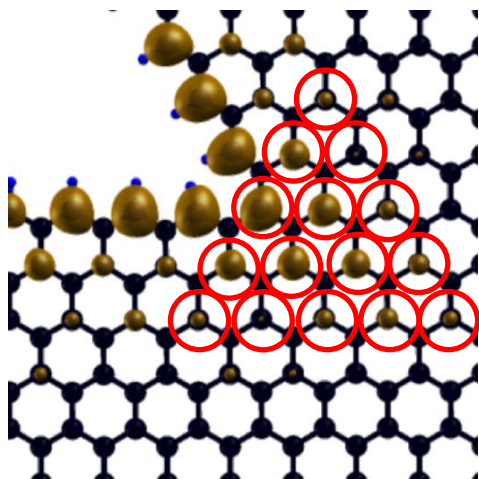


(e)

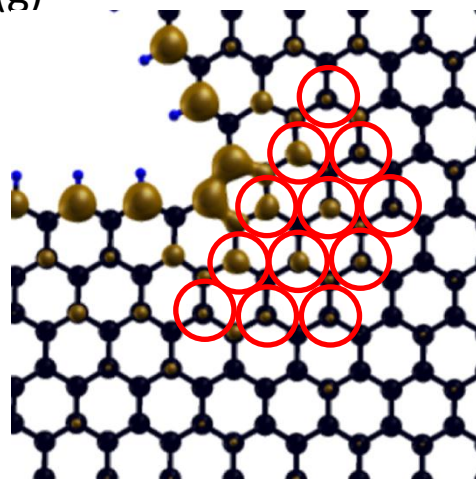
Page 30 of 31



(f)



(g)



(h)

